

How does riming influence the observed spatial variability of ice water in mixed-phase clouds?

Nina Maherndl¹, Manuel Moser^{2,3}, Imke Schirmacher⁴, Aaron Bansemer⁶, Johannes Lucke^{3,5}, Christiane Voigt^{2,3}, and Maximilian Maahn¹

¹Leipzig Institute of Meteorology (LIM), Leipzig University, Leipzig, Germany

²Institute for Physics of the Atmosphere, Johannes Gutenberg University, Mainz, Germany

³Institute for Physics of the Atmosphere, German Aerospace Center (DLR), Wessling, Germany

⁴Institute for Geophysics and Meteorology, University of Cologne, Cologne, Germany

⁵Faculty of Aerospace Engineering, Delft University of Technology, Delft 2629, the Netherlands

⁶NSF National Center for Atmospheric Research, Boulder, Colorado, USA

Correspondence: Nina Maherndl (nina.maherndl@uni-leipzig.de)

Abstract.

Mixed-phase clouds (~~MPC~~MPCs) are a key component of the Earth's climate system. Observations show that the ice water content (IWC) ~~is not distributed homogeneously in MPC~~in MPCs is not homogeneously distributed. Instead, high IWC tends to occur in clusters. However, it is not sufficiently understood which ice crystal formation and growth processes play a dominant role in IWC clustering in clouds. One important ice growth process is riming, which occurs when liquid water droplets freeze onto ice crystals upon contact. Here ~~we use~~ airborne measurements of ~~MPC~~MPCs in mid- and high-latitudes ~~are used to study to investigate the~~ spatial variability of ice clusters in clouds and ~~investigate~~ how this variability is linked to riming. We use data from the IMPACTS (mid-latitudes) and the HALO-(AC)³ (high-latitudes) aircraft campaigns, where spatially and temporally collocated cloud radar and in situ measurements were collected. We derive riming and IWC by combining cloud radar and in situ measurements. Ice cluster scales and IWC variability in clouds are quantified using pair correlation functions. By comparing IWC calculations accounting for riming ~~to~~with IWC calculations neglecting riming, we single out the influence of riming.

During all analyzed flight segments, riming is responsible for 66 % and 63 % of the total IWC during IMPACTS and HALO-(AC)³, respectively. In mid-latitude ~~MPC~~MPCs, riming does not significantly change IWC cluster scales, but increases the probability of clusters occurrence. This enhancement occurs at similar spatial scales as liquid water content variability. In cold air outbreak ~~MPC~~MPCs observed during HALO-(AC)³, riming impacts IWC clustering at two distinctive scales. First, riming enhances the probability of in-cloud IWC clusters at spatial scales below 2 km, which corresponds to the wavelength of the roll cloud updraft and circulation features. Second, riming leads to additional in-cloud IWC clustering at spatial scales of 3-5 km. We find that the presence of mesoscale updraft features leads to enhanced occurrences of riming and therefore additional IWC clustering. An increased liquid water path might increase the effect, but is not a necessary criterion. These

results help to improve our understanding of how riming is linked to IWC variability in clouds and can be used to evaluate and constrain models of MPCs.

25 1 Introduction

In mid- and high-latitudes, most precipitation stems from ice containing clouds (Mülmenstädt et al., 2015), which are a crucial component of the Earth’s weather and climate systems. In mixed-phase clouds (~~MPC~~MPCs), ice particles and supercooled liquid droplets coexist in a thermodynamically unstable state down to temperatures of about $-38\text{ }^{\circ}\text{C}$ ~~in a thermodynamically unstable state~~. The Mass and the ratio of ice and liquid particles play a critical role not only in precipitation processes, but also cloud lifetime, radiative budget (Sun and Shine, 1994; Shupe and Intrieri, 2004; Turner, 2005), and climate feedbacks (Choi et al., 2014; Bjordal et al., 2020).

Numerical forecast and climate models often fail to realistically predict or reproduce MPC properties, ~~lifetime~~lifetimes and precipitation amounts (Morrison et al., 2012, 2020; Ong et al., 2024; Connelly and Colle, 2019). The misrepresentation of ~~MPC~~MPCs and ice clouds has been suggested as ~~large a major~~ contributor to the uncertainty in Coupled Model Intercomparison Project version 6 (CMIP6) climate model predictions (e.g., Bock et al., 2021). This is ~~in part linked~~partly related to a poor understanding of ice formation and growth processes in ~~MPC~~MPCs (Korolev et al., 2017). Their representations are therefore likely incomplete, even in sophisticated cloud microphysics schemes (e.g., Cao et al., 2023), such as the predicted particle properties (P3) scheme proposed by Morrison and Milbrandt (2015). Gaps in our understanding of ~~dominating ice processes hamper progression in representing MPC~~the dominant ice processes hinder progress in the representation of MPCs in models (Morrison et al., 2012).

~~One~~An important ice growth process is riming, which describes the process ~~of supercooled droplets freezing by which supercooled droplets freeze~~ onto ice particles after contact. Riming efficiently converts liquid to ice and typically ~~leads to~~results in increased particle mass, density, and fall speed (Heymsfield, 1982; Erfani and Mitchell, 2017; Seifert et al., 2019). Although riming can theoretically significantly increase ice water content (IWC) in ~~MPC~~MPCs, it is unclear how much it ~~actually~~ contributes to ice mass ~~in reality~~ and further to snowfall amounts on the ground with different studies reaching different conclusions (Harimaya and Sato, 1989; Moisseev et al., 2017; Kneifel and Moisseev, 2020; Fitch and Garrett, 2022; Waitz et al., 2022).

Cloud properties are ~~not only determined~~determined not only by the mass and the ratio of liquid and ice particles, but also by their spatial distribution. Observations show that ice particles and liquid droplets in ~~MPC are often mixed heterogeneously~~MPCs are often heterogeneously mixed, leading to the formation of hydrometeor clusters (Korolev et al., 2003; Field et al., 2004; Korolev and Milbrandt, 2022). The ability to quantify spatial scales of IWC clustering would allow for model ~~evaluations beyond comparing distributions of IWC~~. ~~Additionally, evaluation beyond comparison of IWC distributions. Furthermore, it is poorly understood~~ which microphysical processes lead to IWC clustering at which spatial scales ~~is poorly understood~~. While quantifying spatial scales of cloud particle clusters has been the focus of previous studies, most ~~have~~ focused on liquid-phase clouds ~~and analyzed~~, analyzing liquid droplet clustering on small scales below 1 m (Kostinski and Shaw, 2001; Shaw et al., 2002; Baker and Lawson, 2010), where turbulence plays a major role in clustering (Wood et al., 2005; Saw et al., 2012a, b). Studies ~~looking at MPC~~of MPCs suggest that ice clustering ~~is present~~occurs at different spatial scales than liquid clusters (Korolev and Milbrandt, 2022; Deng et al., 2024). Deng et al. (2024) propose that ice clusters—defined as regions with

enhanced ice particle number or IWC—on larger scales of a few km dominate the inhomogeneity of the ice distribution within clouds. However, their analysis is based on in situ data ~~of from~~ a single case over China, and it is unclear ~~, if whether~~ their findings are representative ~~for of~~ different types of MPCMPCs.

Accurate in situ measurements of IWC remain challenging (Heymsfield et al., 2010; Baumgardner et al., 2017; Tridon et al., 2019), ~~even though although~~ in situ cloud probes can provide reliable particle size distribution (PSD) data (Korolev et al., 2013; Moser et al., 2023). Lacking IWC measurements, Deng et al. (2024) calculated IWC from PSD observations, assuming that ice particle mass as a function of ice particle size follows a power law ~~relation . Because deriving relationship. Because it is difficult to derive~~ size-resolved ice particle densities from in situ ~~PSD alone is not possible yet (to our knowledge) observations alone~~, Deng et al. (2024) used constant mass-size ~~parameter parameters~~ from Heymsfield et al. (2010). Therefore, their ~~analyses analysis~~ captures IWC variability due to ice number concentration and size, but not ice particle density, which is commonly linked to riming (Erfani and Mitchell, 2017; Seifert et al., 2019).

~~Combining The combination of~~ collocated cloud radar and in situ PSD data ~~allows to estimate IWC by not only showing shows~~ great potential to ~~gain better insight on provide better insight into~~ microphysical processes (Nguyen et al., 2022; Mróz et al., 2021), ~~but also to infer. It also allows the estimation of IWC by inferring~~ ice particle density changes due to riming (Maherndl et al., 2024). ~~This In this~~ way, IWC variability driven by riming-induced changes in ice particle density can be studied. In recent years, the synergistic ~~employment use~~ of both remote sensing and in situ instrumentation during airborne campaigns has become more common (Houze et al., 2017; McMurdie et al., 2022; Nguyen et al., 2022; Kirschler et al., 2023; Sorooshian et al., 2023; Wendisch et al., 2024; Maherndl et al., 2024).

Here ~~, we us we use~~ collocated cloud radar and in situ cloud probe observations in MPCMPCs collected during the IMPACTS (McMurdie et al., 2022) and the HALO-(AC)³ (Wendisch et al., 2024) aircraft campaigns. The focus of IMPACTS was to study precipitation variability ~~in during~~ wintertime snowstorms. The main objective of the HALO-(AC)³ campaign was ~~studying to study~~ Arctic air mass transformations ~~during warm air intrusions and marine cold air outbreaks (MCAOs)~~. During both campaigns, two aircraft flew in an approximately vertically stacked coordinated pattern to collect spatially and temporally collocated radar and in situ data.

We aim to:

1. Quantify spatial scales of ice clusters in MPCMPCs observed during the IMPACTS (mid-latitude winter storms) and HALO-(AC)³ (Arctic MCAO clouds) aircraft campaigns.
2. Characterize spatial scales at which riming enhances in-cloud ice clustering and link to drivers of riming.
3. Compare ice cluster scales and the impact of riming for mid- and high-latitude MPCMPCs.

Because we aim to compare IWC variability in MPCMPCs at different latitudes, we ~~are using use~~ data from both aircraft campaigns. IMPACTS data ~~was were~~ collected during four flights over the US East Coast and the Midwest. For HALO-(AC)³, ~~We we~~ use data from three flights over the Fram Strait west of Svalbard. We compare the contribution of riming to IWC to other ice formation processes ~~absolutely in absolute terms~~ and with respect to the spatial scales of ice clustering using the pair

correlation function. The paper is organized as follows: ~~Section 2 introduces~~ Sect. 2 presents the airborne data sets we use to study riming and IWC variability. ~~Section~~ Sect. 3 illustrates the methods we use to quantify riming, derive IWC, and analyze scales of IWC variability in clouds. The main results are presented in Sect. 4. In Sect. 5 we summarize and discuss our findings.

95 2 Data

2.1 Airborne campaigns: IMPACTS and HALO-(AC)³

The Investigation of Microphysics and Precipitation for Atlantic Coast-Threatening Snowstorms (IMPACTS, McMurdie et al., 2022) campaign was a ~~NASA-sponsored~~ National Aeronautics and Space Administration (NASA) sponsored field campaign to study wintertime snowstorms with a focus on precipitation variability in East Coast cyclones. Here, we use data collected
100 during the winter of 2020, where a variety of storms from the Midwest to the East Coast were sampled.

The ~~DFG-funded~~ German Research Foundation (DFG) funded field campaign HALO-(AC)³ (~~Wendisch et al., 2024~~) (Wendisch et al.; HALO, High Altitude and Long Range Research Aircraft – (AC)³ Project on Arctic Amplification Climate Relevant Atmospheric and Surface Processes and Feedback Mechanisms; see <https://halo-ac3.de/>, last access: 8 October 2024) took place in March and April 2022 and aims ~~at investigating warm air intrusions and cold air outbreaks in the Arctic to investigate~~
105 Arctic air mass transformations. In this study, we analyze data collected during MCAO conditions over the Fram Strait west of Svalbard.

~~Both aircraft campaigns have in common that~~ Common to both aircraft campaigns was the use of two aircraft to perform collocated in situ and remote sensing measurements ~~were conducted with two aircraft~~. During IMPACTS, the *ER-2* aircraft flew above clouds carrying a variety of passive and active remote sensing instruments including ~~multiple frequency~~ multi-frequency
110 Doppler radars. Simultaneously, the NASA *P-3* aircraft collected measurements of microphysical cloud properties in situ while flying ~~within~~ inside clouds. During HALO-(AC)³, the AWI aircraft *Polar 5* and *Polar 6* ~~conducted measurements in a similar manner~~ performed similar measurements. *Polar 5*, equipped with a W-band radar among other remote sensing instruments, flew above *Polar 6*, which ~~carried out~~ performed in situ measurements in clouds.

However, both campaigns ~~cover~~ covered different observation areas and sampled at different frequency rates, i.e. τ -different
115 spatial resolutions. With a typical flight speed of 200 (150) m/s the *ER-2* (*P-3*) ~~eovers~~ covered a larger spatial scale ~~at with~~ a coarser resolution than *Polar 5* and *Polar 6*, which flew at 60–80 m/s. While the *ER-2* and *Polar 5* flew at ~~constant altitudes a~~ constant altitude of 20 km and 3 km, respectively, *P-3* and *Polar 6* sampled at different altitudes up to 8.5 and 3 km, respectively. In this study, we investigate data collected during the flight days listed in Tab. 1. We selected these days because of the good collocation (which we define as maximum spatial offsets of 5 km and temporal offsets of 5 min; see Sect. 2.4) between the
120 respective remote sensing and in situ aircraft ~~as well as the~~ and because of data availability. Figure 1 shows all coordinated flight ~~paths~~ tracks.

2.2 Instruments

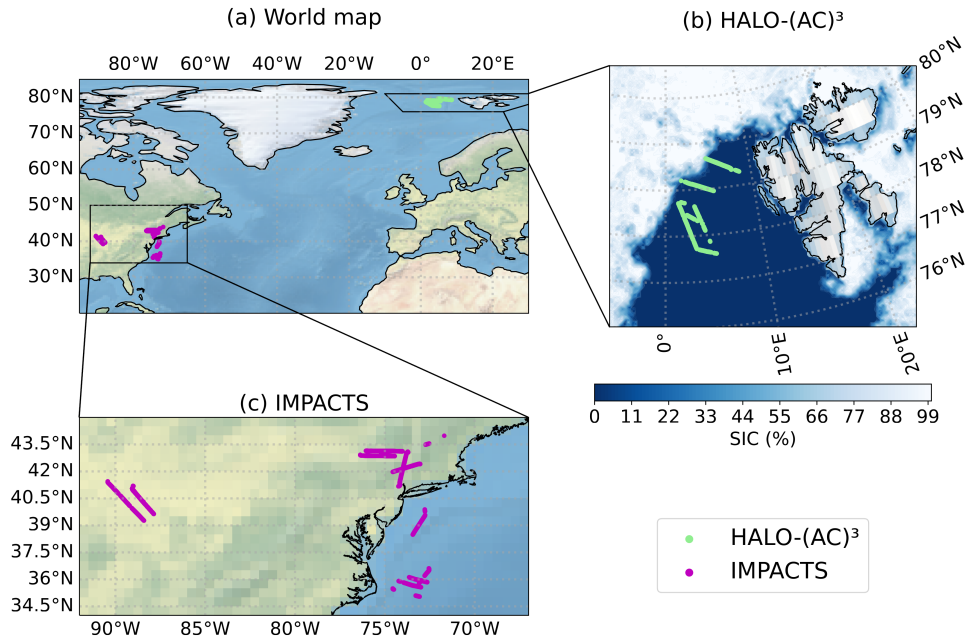


Figure 1. Flight tracks of (a) all analyzed coordinated flight segments, zoomed in on (b) HALO-(AC)³, and (c) IMPACTS measurement area. In (b) the sea ice concentration (SIC) derived from the Advanced Microwave Scanning Radiometer 2 (AMSR2) onboard the GCOM-W1 satellite on 1 April 2022 is shaded in blue.

Table 1. Overview of analyzed flight days including campaign, measurement area, and synoptic situation.

Campaign	Flight day	Measurement area	Synoptic situation / mission target
IMPACTS	25 January 2020	East Coast, New York	Warm occluded front
IMPACTS	1 February 2020	East Coast, Atlantic	Warm developing frontal system
IMPACTS	5 February 2020	Midwest	Shallow frontal zone
IMPACTS	7 February 2020	East Coast, Albany	Rapidly deepening cyclone
HALO-(AC) ³	28 March 2022	Fram Strait	MCAO
HALO-(AC) ³	1 April 2022	Fram Strait	MCAO
HALO-(AC) ³	4 April 2022	Fram Strait	MCAO

Equivalent The equivalent radar reflectivity factor Z_e was measured by multiple radars during IMPACTS: X-band (9.6 GHz, EXTRAD, Heymsfield et al., 1996, 2022), Ku and Ka-band (13.6 and 35.6 GHz, HIWRAP, Li et al., 2016, 2022), and W-band (94 GHz, CRS, McLinden et al., 2021, 2022). EXTRAD consists of a nadir-pointing and a conically scanning beam, however, we only use but only the nadir-pointing beam is used in this study. EXTRAD, HIWRAP, and CRS sampled at 4 Hz, 2 Hz, and 4 Hz at with vertical resolutions of 19 m, 26 m, and 26 m, respectively. EXRAD, HIWRAP Ku-band, HIWRAP Ka-band, and

CRS have sensitivity limits of -15 dBZ, 0 dBZ, -5 dBZ, and -28 dBZ at 10 km range, respectively. During HALO-(AC)³, a W-band radar (94 GHz, MiRAC-A, Mech et al., 2019; Mech et al., 2024a) was deployed. MiRAC-A was mounted with a 25° backwards inclination, sampled at 1 Hz and Z_e data ~~is~~are available with 5 m vertical resolution. For ~~scattering calculations done~~the scattering calculations performed within this study, the 25° inclination is negligible (not shown). MiRAC-A has a sensitivity limit of about -40 dBZ at 3 km range. For both campaigns, Z_e data ~~is~~are quality controlled and corrected for instrument orientation and aircraft motion (for MiRAC-A, see Mech et al., 2019). Uncertainties of Z_e ~~stemming from~~due to radar calibration are estimated to be below 1 dB and 0.5 dB for IMPACTS and HALO-(AC)³ data, respectively (Finlon et al., 2022; Mech et al., 2019). MiRAC-A Z_e is corrected for attenuation due to liquid water content (LWC) as described in Mahernndl et al. (2024); CRS Z_e as described in Finlon et al. (2022). Attenuation due to water vapor and atmospheric gases is below 0.5 dB for all radars and therefore neglected.

During HALO-(AC)³, brightness temperature T_B measurements at 89 GHz were collected and are used to derive the ~~LWP~~liquid water path (LWP). Differences in T_B for clear-sky and cloudy ~~situations~~conditions are used to retrieve LWP over ~~the open~~ ocean via a regression approach (Ruiz-Donoso et al., 2020; Mahernndl et al., 2024). Lidar measurement of backscattered intensities at 532 nm (parallel and perpendicular polarized) and 355 nm (~~not polarized~~non-polarized; Stachlewska et al., 2010) are used to derive cloud top height (CTH) during HALO-(AC)³ (Mech et al., 2022a; Schirmacher et al., 2023; Mahernndl et al., 2024; Mech et al., 2024b).

Cloud particle observations obtained with a variety of cloud probes cover a size range from 2 μm to about 2 cm for IMPACTS and 2.8 μm to 6.4 mm for HALO-(AC)³. For IMPACTS, we use data from a Fast-Cloud Droplet Probe (Fast-CDP, 2-50 μm , Lawson et al., 2017), a Two-Dimensional Stereo (2D-S, Lawson et al., 2006) probe (10-2000 μm , pixel resolution of 10 μm), one horizontally, and one vertically oriented High Volume Precipitation Spectrometer, version 3, (HVPS-3, Lawson et al., 1998) probe (0.3-19.2 mm, pixel resolution of 150 μm). For HALO-(AC)³, we use data from a Cloud Droplet Probe (CDP, 2.8-50 μm , Lance et al., 2010), a Cloud Imaging Probe (CIP, 15-960 μm , pixel resolution of 15 μm , Baumgardner et al., 2001), and a Precipitation Imaging Probe (PIP, 103-6400 μm , pixel resolution of 103 μm , Baumgardner et al., 2001). Here, we use merged particle size distribution (PSD) data from the respective campaign (Bansemmer et al., 2022; Moser et al., 2023), which are derived from the instruments listed above. As in Moser et al. (2023) and Mahernndl et al. (2024), we assume all particles larger than 50 μm in MPC-MPCs to be ice ~~crystals~~particles. As in Mahernndl et al. (2024), we only include data up to -1 °C to avoid melting ~~effects~~ice particles, which are not represented well in the scattering simulations that we perform. In addition, we manually looked through in situ images of all ~~analyzed~~remaining flight segments and removed two IMPACTS segments, where we could identify supercooled droplets larger than 50 μm . LWC was measured in situ with a King probe (King et al., 1978) and a Nevzorov probe (Korolev et al., 1998; Lucke et al., 2022; Lucke et al., 2024) during IMPACTS and HALO-(AC)³, respectively. Due to poor data availability¹ and high uncertainties of IWC measurements, IWC is calculated from the PSD as described in more detail in Sect. 3.2. For more ~~detail~~details on IMPACTS and HALO-(AC)³ instrumentation

¹IMPACTS (2020): Water Isotope System for Precipitation and Entrainment Research (WISPER, Toohey et al., 2022) data product is available but unreliable under riming / icing conditions; HALO-(AC)³: Nevzorov probe data product only for April flights

160 and data processing, we refer the reader to McMurdie et al. (2022) and Moser et al. (2023), Mech et al. (2022a), as well as
Maherndl et al. (2024), respectively.

2.3 Synoptic situation

In this section, we give a brief overview of the "~~typical~~" typical synoptic situations encountered during the different field
campaigns to provide context ~~on~~ for the types of ~~MPC~~ MPCs that we analyze. We use ~~one~~ an example flight segment for each
165 campaign, which we describe in detail in Sect. 4.1.1 and 4.1.2.

During IMPACTS, ~~observations of~~ a variety of mid-latitude wintertime storms in different development stages were ~~conducted~~ observed.
The focus was on ~~observing the observation of~~ banded precipitation structures. Observations range from a relatively weak and
warm developing Atlantic low systems without major banding structures (1 February 2020) to rapidly deepening cyclones with
significant snowfall and snowbands (5 February 2020). The majority of ~~the~~ measurements stem from the U.S. Midwest, and
170 close to the East Coast (both over ocean and land), ranging up to southern parts of Canada (Fig. 1). The coordinated *ER-2* and
P-3 flights on 5 February sampled an elevated warm front over shallow, pre-existing cold air as a low pressure center developed
over Louisiana and Mississippi. The developing circulation around the low produced a low-level northeasterly flow across the
Midwest. ~~Due to the overrunning warm moist air from the south, precipitation in the form of rain (to~~ Precipitation formed as
rain (in the south) and snow (to ~~in the north) formed~~ due to the overflow of warm, moist air from the south. During the ~~period~~
175 ~~of observations~~ observation period, snowband structures were observed.

Measurements during HALO-(AC)³ were conducted west of Svalbard over both open ocean and sea ice. However, clouds
~~over the sea ice~~ were very thin to non-existent ~~over sea ice~~ during all three flights used here. Northerly to northeasterly flow
brought cold air masses from the sea ice of the higher Arctic to the comparatively warm open ocean. This led to the formation
of roll cloud streets. ~~During~~ On 1 April 2022 the MCAO was especially strong ~~meaning the difference of the potential, i.e. the~~
180 ~~difference between the potential temperature~~ at sea surface and the potential temperature at 850 hPa was large (about 8 K);
~~while during~~. On 28 March and 4 April 2022 weaker MCAO conditions were observed due to ~~air masses being convected~~
~~convection of air masses~~ from North America over Siberia (28 March) or the central Arctic (4 April) to Svalbard (Walbröl
et al., 2024).

2.4 Collocation

185 To combine in situ and remote sensing observations of the two aircraft, we use the same collocation criterion as in Maherndl
et al. (2024), which is also extended to the IMPACTS data. ~~To summarize, the nearest~~ In summary, following Chase et al. (2018)
and Nguyen et al. (2022), the closest radar data point to the in situ measurements is selected ~~following Chase et al. (2018) and~~
~~Nguyen et al. (2022)~~. Each 1 Hz, 2 Hz, or 4 Hz radar aircraft (*Polar 5* and *ER-2*) data point is matched with the spatially closest
in situ aircraft (*Polar 6* and *P-3*) data point within a 5 min time window. We consider data with ~~maximum spatial offsets a~~
190 ~~maximum spatial offset~~ of 5 km ~~as to be~~ "collocated". The closest radar range gate to the flight altitude of the in situ aircraft is
chosen. Averaging over certain height ranges did not lead to significant improvements.

Rolling averages were applied to Z_e and in situ data to obtain more robust statistics for the latter. To cover approximately the same spatial scales, averaging windows of 10 s and 30 s are chosen for IMPACTS and HALO-(AC)³, respectively. With typical flight speeds of 180-200 m/s and 60-80 m/s during IMPACTS and HALO-(AC)³, respectively, this corresponds to spatial scales of 1.8-2.0 km and 1.8-2.4 km, [respectively](#). We assume the in situ measurement is representative of the entire matched radar volume. Possible implications of this assumption ~~on~~ [for](#) the riming retrieval are discussed in Maherndl et al. (2024).

3 Methods

3.1 Retrieving ice particle riming

We use the normalized rime mass M (Seifert et al., 2019) to describe riming. M is defined as the particle's rime mass m_{rime} divided by the mass of a size-equivalent spherical graupel particle m_g , where we assume a rime density of $\rho_{\text{rime}} = 700 \text{ kg m}^{-3}$:

$$M = \frac{m_{\text{rime}}}{m_g}, \quad (1)$$

where

$$m_g = \frac{\pi}{6} \rho_{\text{rime}} D_{\text{max}}^3. \quad (2)$$

The maximum dimension D_{max} is defined as the diameter of the smallest circle encompassing the cloud particle in m and is used to parameterize particle sizes.

We retrieve M using the two methods introduced in Maherndl et al. (2024), which are termed the *combined method* and the *in situ method*. The methods in Maherndl et al. (2024) were developed for HALO-(AC)³, but we apply them to IMPACTS data with slight adjustments due to different instrumentation. In the following, we give a brief explanation of both methods and describe the adjustments for IMPACTS data. For more [detail](#)[details](#), we refer the reader to Maherndl et al. (2024).

The combined method derives M along the flight track of the in situ airplane from collocated PSD and radar reflectivity Z_e measurements. It therefore relies on collocated in situ and remote sensing flights. An Optimal Estimation (Rodgers, 2000) algorithm is used to retrieve M by matching simulated radar reflectivities Z_e obtained from observed in situ PSD with the spatially and temporally closest measured Z_e . As forward operator we use the Passive and Active Microwave radiative TRAnSfer tool (PAMTRA, Mech et al., 2020), which includes empirical relationships Maherndl et al. (2023a) for estimating particle scattering properties as a function of M . For IMPACTS, the combined method is applied (separately) to X-, Ku-, Ka- and W-band Z_e (see Sect. 4.1.3). As in Maherndl et al. (2024), we use the [riming-dependent](#)[riming-dependent](#) mass-size parameter relation for dendrites from Maherndl et al. (2023a) that were estimated for different degrees of riming, i.e. M values. Dendrites were chosen, because 86.2 % of [the](#) data during the analyzed IMPACTS segments are within [the](#) temperature ranges of -20 °C to -10 °C and -5 °C to 0 °C, where plate-like growth of ice crystals is [preferred](#)[favored](#) (only 13.8 % of the data [he](#) [are](#) between -10 °C and -5 °C, where column-like growth dominates). We assume dendrite shapes for the [whole dataset](#), [because of](#) [entire dataset](#)

for two reasons. First, Maherndl et al. (2024) found that assuming plates or dendrites gives the same results within uncertainty estimates, and second, we want to keep the analysis of IMPACTS and HALO-(AC)³ data as consistent as possible.

225 The in situ method uses in situ measurements of ice particle area A , perimeter P , and D_{\max} to derive M for individual ice particles, from which an average M for the particle population is derived. The in situ method is applied to 2D-S and HVPS-3 data for IMPACTS as was done using with CIP and PIP data for HALO-(AC)³ in Maherndl et al. (2024). P and A measurements in pixel are used to calculate complexity $\chi = \frac{P}{2\sqrt{\pi A}}$. Simulated rimed aggregates from Maherndl et al. (2023b) are used to derive empirical functions relating χ and D_{\max} to M , where χ and D_{\max} are derived using the same processing

230 steps as for the respective cloud probes. Because these processing steps were slightly different for 2D-S and HVPS-3 operated during IMPACTS² than for CIP and PIP during HALO-(AC)³, new fit functions (based on 18352 simulated dendrites; with $R^2 = 0.92$) had to be derived for IMPACTS:

$$\log_{10}(M) = \frac{1.11 - \chi + 0.00141 \cdot D_{\max}}{0.00432 \cdot D_{\max} + 0.218}. \quad (3)$$

Only a subset of ice particles can be used to derive M with the in situ method, because particles cannot touch edges to derive P and need to must be large enough to derive meaningful χ . We therefore assume Because of these two criteria, ice particles with D_{\max} in the range of about 1.0-1.4 mm and 2.0-6.0 mm are neglected by the in situ method when using the HALO-(AC)³ and IMPACTS particle probes, respectively. Therefore, we assume that the combined method—which uses the full PSD—gives more reliable results when if the aircraft are reasonably collocated. In situ method results are therefore only shown, as shown in Maherndl et al. (2024) for HALO-(AC)³. We use M derived with the combined method for all further

240 analysis steps. For reference and uncertainty estimation, we show the in situ method M results are in Sect. 4.1.1 and 4.1.2 as references and the combined method is used in all further analysis steps and in Appendix A.

3.2 Deriving ice water content (IWC)

IWC is calculated by summing the product of ice particle mass $m(D_{\max})$ and $N(D_{\max})$ for the probes²—lower to upper size ranges of the probes, D_{lower} to D_{upper}

$$245 \quad IWC = \sum_{D_{\text{lower}}}^{D_{\text{upper}}} m(D_{\max})N(D_{\max})\Delta D_{\max}, \quad (4)$$

where ΔD_{\max} is the size bin width. $m(D_{\max})$ is approximated by a power law relation with prefactor a_m and exponent b_m

$$m(D_{\max}) = a_m D_{\max}^{b_m}. \quad (5)$$

a_m scales the density of ice particles (independent of particle size) and b_m modulates the size dependency-dependence of particle mass, which is related to particle shape and growth processes. a_m and b_m depend strongly on riming (e.g., Mitchell, 1996) and reported literature values—values in the literature range from 0.0058 to 466 for a_m and 1.8 to 3.0 for b_m in SI units

250

²The number of perimeter pixel P is computed by the sum of all pixel that are pixels eroded when applying a "+" shaped erosion kernel without performing dilation/erosion sequences as was done during HALO-(AC)³.

(e.g., discussed by Mason et al., 2018). As shown by Mahernndl et al. (2023a), a_m and b_m strongly depend on the amount of riming, which increases particle densities. Mahernndl et al. (2023a) provide a_m and b_m values for discrete M , which are ~~interpolate~~ interpolated in this study to obtain parameters for a continuous M ~~in this study~~. We derive a_m and b_m for each time step as a function of the retrieved M . IWC is then calculated ~~with-using~~ Eq. 4 for each time step based on the measured PSD
 255 and the derived a_m and b_m parameters. We refer to this quantity as IWC_r (IWC accounting for riming).

To estimate the contribution of the riming process to IWC, we also calculate IWC using fixed mass-size parameters a_m and b_m for unrimed particles (also taken from Mahernndl et al., 2023a), thereby neglecting density changes (e.g., due to riming). We ~~refer to call~~ this quantity as IWC_u . IWC_u can be seen as the "theoretical" IWC, if the ice particles were unrimed, so that the riming contribution can be estimated from the difference between IWC and IWC_u . However, this implies that riming does
 260 not ~~impact-affect~~ the size of the unrimed ice particle, which is not necessarily the case in nature. Riming typically ~~not-only~~ leads-leads not only to an increase in ice particle density, but also ice particle size (Seifert et al., 2019). Therefore, we likely underestimate the contribution of riming to particle mass when comparing IWC_u ~~with-to~~ IWC. Since we are interested in the contribution of riming to IWC variability, this approach likely results in a conservative estimate of the contribution of riming to IWC variability.

265 3.3 Characterizing scales of IWC variability in clouds

Similar to Deng et al. (2024), we use the pair correlation function (PCF) to quantify the spatial inhomogeneity of ice water in the observed clouds. In discrete systems, the PCF describes the degree of deviation from the homogeneous Poisson process. In clouds, the PCF can be used to quantify the degree of clustering or variability of a certain parameter such as the number concentration of liquid droplets, the number concentration of ice particles, LWC, or IWC (e.g., Shaw et al., 2002; Saw et al.,
 270 2012a; Deng et al., 2024). The PCF applied to a one-dimensional parameter p is given by:

$$\eta(r) = \frac{\overline{p(0)p(r)}}{(\bar{p})^2} - 1, \quad (6)$$

where $p(0)$ is the parameter at a given point, $p(r)$ is the parameter at the lag r from that point, and \bar{p} is the average of p (Kostinski and Jameson, 2000; Shaw et al., 2002). Thus, $\eta(r)$ is a measure ~~for the probability to find of the probability of finding~~ clusters of p as a function of lag r compared to \bar{p} . Positive values indicate the ~~occurrence-presence~~ of clusters and the
 275 higher $\eta(r)$, the higher the probability ~~to find of finding~~ clusters at that scale. If p follows a homogeneous Poisson distribution, which PCF assumes to be statistically homogeneous, $\eta(r) = 0$. Negative values indicate that ~~at the given scale, it is less likely to find clusters~~ the probability of finding clusters at that scale is lower than on average ~~over-for~~ the whole segment.

In this study, only straight flight segments with a minimum of 200 s of continuous in-cloud measurements are used to calculate $\eta(r)$. The respective radar sensitivity limits are used to define "in-cloud". We allow measurement gaps with a maximum
 280 length of 5 s, which are linearly interpolated. Table 2 gives an overview of all segments we analyze, including duration and data amount. Because IWC is derived using running averages of 10 s and 30 s for IMPACTS and HALO-(AC)³ data, respectively, we investigated the impact of the window size of the moving average on $\eta(r)$. We found that ~~while~~ increasing the window size from 1 s to 10 (30) s for IMPACTS (HALO-(AC)³) decreases ~~absolute values~~ the absolute value of $\eta(r)$, ~~at which lags~~

285 However, the lags r at which $r \eta(r)$ is positive does not change (not shown). This is because applying a moving average
smooths peaks in the 1 Hz signal, but does not necessarily change their periodicity as long as the window size is reasonably
small.

Additionally, we use power spectra in order to gain insight on-into scales of variability of CTH and LWP during HALO-
(AC)³. To do so this, each data segment is mean-centered and linearly detrended. To minimize edge effects, a Hann window
is applied to each segment to minimize edge effects. Frequency is converted to wavelength using the aircraft speed v_{air} . With
290 a minimum time range of 200 s per segment, we capture spatial scales of 12 km for HALO-(AC)³ meaning that we do not
capture synoptic-scale motions. We interpret results up to 0.1 Hz meaning, i.e. spatial scales of 600 m.

Figure 2 visualizes the PCF and power spectra for synthetic data. In the case of For a homogeneous Poisson process (Fig.
2a), $\eta(r) = 0$ (Fig. 2d) and the power spectral density shows no significant peaks (Fig. 2g). For a periodic sine function with
added Poisson noise Poisson noise added (Fig. 2b), $\eta(r)$ is positive for small lags and oscillates around 0 for larger lags with
295 peaks occurring at multiples of the wavelength λ of the sine function (Fig. 2e). The power spectrum shows a peak at λ (Fig.
2h). If When the modulus function is applied to the sine curve (Fig. 2c), $\eta(r)$ (Fig. 2f) is smaller than in Fig. 2e due to the
lower signal-to-noise ratio signal-to-noise ratio, and the oscillation occurs at $\lambda/2$. The power spectrum also shows a peak at $\lambda/2$
(Fig. 2i).

4 Results and discussion

300 To characterize the influence of riming on the spatial variability of ice clusters in clouds, we first need to know the amount of
riming as well as and its impact on IWC and second. Second, we need to know spatial IWC cluster scales with and without
riming. Therefore, this section is structured as follows. First, we quantify the amount of riming observed during the two
analyzed both campaigns (Sect. 4.1). Then, we show that the retrieved amounts of riming have a significant impact on IWC
(Sect. 4.2). Finally, we quantify in-cloud IWC variability (Sect. 4.3) and discuss the impact of riming on spatial scales and the
305 probability of IWC clusters clustering in clouds.

4.1 Riming occurrence

MPC properties, synoptic situations (Sect. 2.3), and measurement locations (Fig. 1) vary between IMPACTS and HALO-
(AC)³. Clouds during collocated IMPACTS segments have much larger vertical extents than during HALO-(AC)³ segments.
The median CTH during IMPACTS segments is 7.3 km (25-75 % quantile range: 6.3-7.8 km). Here, we define CTH as the
310 height of the highest radar range gate with continuous Z_e above the in situ aircraft altitude.

Clouds observed during collocated HALO-(AC)³ segments were predominately shallow roll clouds that formed during
MCAOs. The maximum CTH during all segments was 2.2 km (25-75 % percentile range: 0.69-1.1 km). Cloud properties
during 1 and 4 April 2022 are described in detail in Schirmacher, et al. (2024).

In the following, we give a brief overview on of the differences in MPCs encountered during between the two campaigns
315 using two "typical" typical example cases. We show a flight segment from 5 February 2020 for IMPACTS (Sect. 4.1.1), and

Table 2. Overview of analyzed segments including campaign, flight day, start and end times in UTC, and number of 1 s data points.

Campaign	Flight day	Segment start	Segment end	Number of data points
IMPACTS	25 January 2020	20:30:37	20:40:04	568
IMPACTS	25 January 2020	21:08:31	21:17:16	526
IMPACTS	25 January 2020	21:41:01	21:53:38	758
IMPACTS	1 February 2020	13:08:48	13:16:47	480
IMPACTS	1 February 2020	14:35:24	14:39:32	249
IMPACTS	5 February 2020	21:05:28	21:10:57	330
IMPACTS	5 February 2020	21:15:47	21:19:27	221
IMPACTS	5 February 2020	21:20:56	21:28:27	452
IMPACTS	5 February 2020	21:49:52	22:04:07	856
IMPACTS	5 February 2020	23:07:26	23:12:40	315
IMPACTS	7 February 2020	15:12:42	15:20:23	462
IMPACTS	7 February 2020	15:35:00	15:48:47	828
IMPACTS	7 February 2020	15:57:02	16:08:11	670
HALO-(AC) ³	28 March 2022	14:10:44	14:18:43	480
HALO-(AC) ³	28 March 2022	14:20:20	14:25:16	287
HALO-(AC) ³	28 March 2022	14:35:07	14:39:33	267
HALO-(AC) ³	28 March 2022	14:41:26	14:45:16	331
HALO-(AC) ³	1 April 2022	11:08:38	11:18:59	622
HALO-(AC) ³	1 April 2022	11:20:38	11:33:02	745
HALO-(AC) ³	1 April 2022	12:07:18	12:14:14	417
HALO-(AC) ³	1 April 2022	12:15:54	12:20:56	303
HALO-(AC) ³	1 April 2022	12:24:57	12:33:38	522
HALO-(AC) ³	1 April 2022	12:34:03	12:39:09	307
HALO-(AC) ³	4 April 2022	11:48:05	12:00:12	728
HALO-(AC) ³	4 April 2022	13:11:48	13:18:24	397
HALO-(AC) ³	4 April 2022	13:19:14	13:30:22	669

from 1 April 2022 for HALO-(AC)³ (Sect. 4.1.2). We present M_{r} -retrieved with combined and in situ ~~method,~~methods and discuss uncertainties. ~~Then, we~~We then extend to data from all collocated segments (Sect. 4.1.3).

4.1.1 Case study 1: Mid-latitude winter storm on 5 February 2020

Figure 3 shows a 64 km segment from 5 February, where *ER-2* and *P-3* ~~were sampling a developing low pressure~~sampled a
320 developing low-pressure system over Illinois from 23:07:26 to 23:12:40 UTC. According to the level-2 MODIS Moderate-resolution

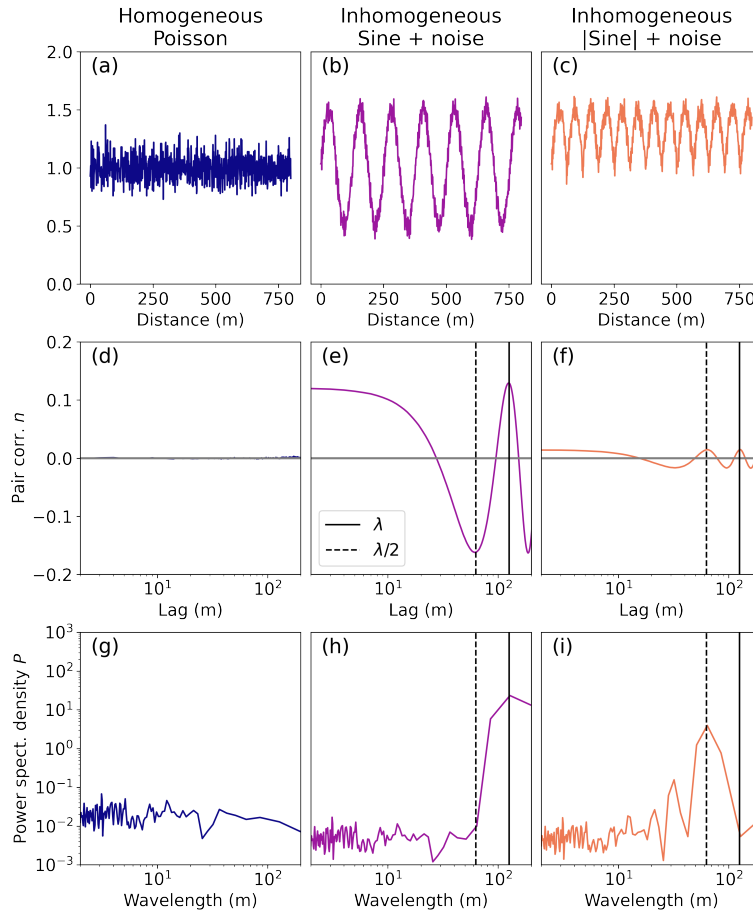


Figure 2. Schematic diagram introducing the pair correlation function (PCF) and power spectral density for (a) a homogeneous Poisson distributed signal, (b) a sine curve with wavelength λ and ~~added~~-Poisson noise ~~added~~, and (c) the same sine curve but mirrored upwards along $x = 1$ to show the impact of λ and signal-to-noise ratio. The respective PCF η as a function of lag is shown in (d)-(f); the power spectra density as a function of wavelength in (g)-(i). The solid and dashed lines indicate λ and $\lambda/2$ of the sine curve in (b).

Imaging Spectroradiometer (MODIS) cloud product (NASA worldview), the cloud top temperature (CTT) was -33 ± 5 °C. W-band Z_e shows the deep cloud with convective cell structures near cloud top from which sheared fall streaks ~~stretch down~~ extend downward (Fig. 3a). P -3 measured the number of ice particles larger than $50 \mu\text{m}$ N_i in the range of 910 m^3 to 2800 m^3 (Fig. 3b). Here we show D_{32} (Fig. 3b), which is the proxy for the mean mass-weighted diameter (e.g., Maahn et al., 2015).
 325 D_{32} is defined as the ratio of the third to the second measured PSD moments (e.g., Mitchell, 1996). During the first 20 km of the segment, ice particles had D_{32} of about 3 mm and were lightly rimed with M of about 0.02 (Fig. 3.c). ~~Afterwards~~Then, D_{32} increases up to 8 mm, indicating aggregates, and M drops below the riming threshold of 0.01. From -88.9°E onward, D_{32} decreases and M increases. Combined method M results using the different frequencies show good agreement between X-, Ku-, and Ka-band. W-band results are likely biased high due to the high D_{32} , as will be discussed in Sect. 4.1.3. IWC

330 is calculated with Eq. 4 using (1) the measured PSD and mass-size parameters a_m and b_m for unrimed particles (blue line) and (2) a_m and b_m based on ~~look-up~~ look-up tables (Maherndl et al., 2023a) for each time step depending on the retrieved M for each frequency (black lines). The derived IWC from Ku-band M varies between 0.015 gm^{-3} and 0.31 gm^{-3} (panel 4). If riming is neglected, i.e. ~~mass-size parameter~~ mass-size parameters for unrimed particles are used in the IWC calculation, IWC is on average lower by a factor of 3.7 lower.

335 The increase in M starting at -88.7°E could be ~~linked-related~~ linked-related to the decrease in CTH (as seen by the radar). Some particles are possibly rimed in liquid layers near cloud top and fall down to the measurement location. On their way down, they might may undergo additional growth processes (condensational growth or aggregation) leading to a decrease ~~of-in~~ of-in M , since M is normalized to particle size. However, King probe measurements show that liquid water also occurs at the $P-3$ position. Therefore ~~additional-riming-can-take-place~~, additional riming may occur at the $P-3$ location and possibly in cloud layers above.

340 2-DS images (Fig. 3) show a change from large, lightly rimed aggregates to small, more heavily rimed particles.

4.1.2 Case study 2: Arctic roll clouds on 1 April 2022

Figure 4 shows a 35 km segment from 1 April, where *Polar 5* and *Polar 6* ~~were sampling~~ sampled perpendicular to the roll cloud structures formed during ~~a-MCAO~~ MCAO conditions over the Fram Strait from 11:20:38 UTC to 11:33:02 UTC (see Maherndl et al., 2024, for a detailed discussion of the case as well as particle images). The MODIS CTT was $-18 \pm 5 \text{ }^\circ\text{C}$.

345 W-band Z_e shows the vertical structure of the individual cloud rolls (Fig. 4a). While *Polar 6* was flying close to cloud top, N_i was high with a maximum of 27300 m^{-3} , while D_{32} was low with a minimum of 0.077 mm (Fig. 4b). ~~Once-As~~ Polar 6 ~~was descending~~ descended, N_i dropped to a minimum of 4600 m^{-3} , while D_{32} increased up to 1.4 mm (panel 2). M oscillates between 0.01 and 0.1 , with peaks occurring in streaks of high Z_e (Fig. 4c). The resulting IWC is between 0.022 gm^{-3} and 0.084 gm^{-3} . This is a factor of 2.8 higher than compared to using a mass-size parameterization for unrimed particles (Fig. 4d).

350 Both methods used to derive M agree well for this segment in terms of M distributions and location and extent of maxima ($R^2 = 0.52$). Statistical agreement between ~~both-the-two~~ both-the-two methods was achieved ~~during-for~~ during-for all HALO-(AC)³ segments used in this study. However, spatio-temporal agreement could not be achieved for inhomogeneous cloud observations (e.g., when *Polar 6* was flying in and out of cloud ~~close-to-near-the~~ close-to-near-the CTH) as discussed in Maherndl et al. (2024).

4.1.3 ~~Campaign-overview~~ Riming product statistics and discussion

355 In the previous section, two case studies were used to show differences between clouds observed during the two campaigns, especially in terms of vertical extent, structure, and riming. ~~In spite-of~~ Despite these differences, normalized rime mass M distributions derived for IMPACTS and HALO-(AC)³ are similar (Fig. 5a, b). Median M for all collocated IMPACTS segments are 0.024 , 0.022 , 0.025 , and 0.034 when derived with ~~X-, Ku-, KaX-, Ku-, Ka-~~ X-, Ku-, KaX-, Ku-, Ka-, and W-band Z_e , respectively. During collocated HALO-(AC)³ segments, median M is 0.024 . For IMPACTS, the ~~disagreement-of-discrepancy-between~~ disagreement-of-discrepancy-between the W-band results ~~to~~ to

360 and the other frequency bands is due to the ~~occurrences~~ occurrence of large ice particle sizes. ~~Due-to-saturation-effects-for~~ Due-to-saturation-effects-for Z_e ~~values-associated-with-large-particles-at-94-GHz~~ values-associated-with-large-particles-at-94-GHz ~~Because of saturation effects~~, the riming-dependent parameterization (Maherndl et al., 2023a) ~~used-here~~ used-here has a positive Z_e bias for ~~size-parameters~~ size-parameters $x = 2\pi\alpha_e D_{max}/\lambda > 4$ where $x > 4$. ~~Here~~ Here ~~large relative sizes~~ large relative sizes

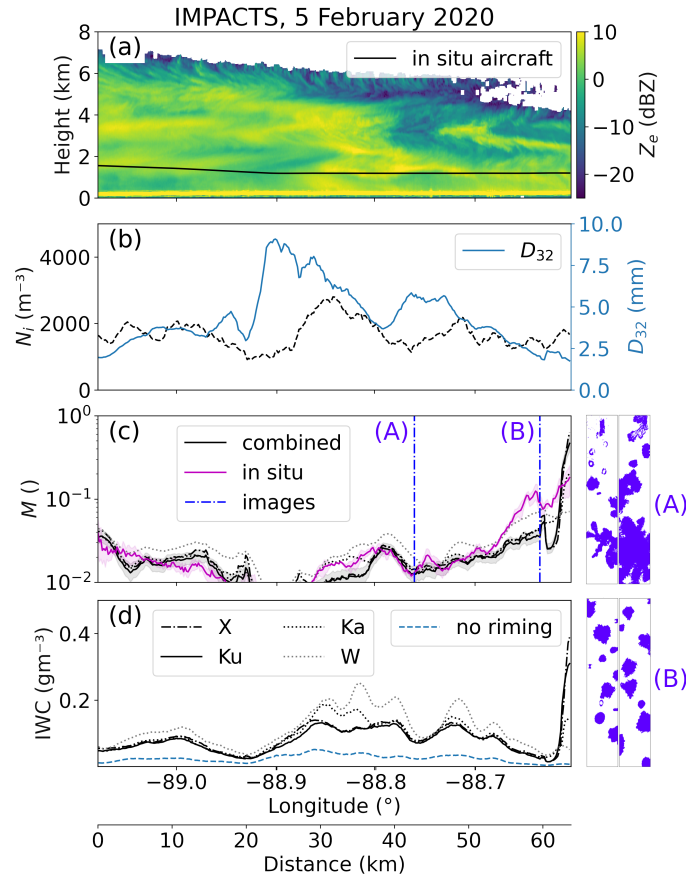


Figure 3. Collocated flight segment from 5 February 2020 at 23:07:26 to 23:12.40 UTC during IMPACTS. (a) W-band radar reflectivity Z_e , and P-3 flight altitude; (b) ice number concentration N_i and mass-weighted diameter D_{32} derived from the 10 s running averaged particle size distribution (PSD); (c) normalized rime mass M from combined (black) and in situ method (magenta) including uncertainty estimates (combined: optimal estimation (OE) standard deviation, in situ: 10 s running standard deviation), where the combined method was applied to X-, Ku-, Ka-, and W-band Z_e (Ku-band results, which are used in the further analysis, are shown as solid lines); (d) ice water content (IWC) derived from the 10 s running averaged PSD and combined method M (black) and assuming $M = 0$ (blue). Combined method results for different radar frequencies are drawn as dashed lines. 2-DS images at (A) -88.78°E and (B) -88.69°E are shown in blue next to panels (c) and (d).

of scattering particles. The relative size of a scattering particle is defined by its size parameter $x = 2\pi\alpha_e D_{max}/\lambda$, where α_e is the ice particle's effective aspect ratio of the ice particle, and λ the radar wavelength. Positive biases occur for $x > 4$.
 365 The positive Z_e bias for $x > 4$ results in a positive bias of M . For IMPACTS, 25% of the data have $D_{32} > 3.2$ mm, which corresponds to $x = 4$ at 94 GHz assuming a typical value of $\alpha_e = 0.6$. Therefore, W-band results for IMPACTS are not as trustworthy as the other wavelengths and are not used in the following analysis. Different to Unlike IMPACTS, the M bias

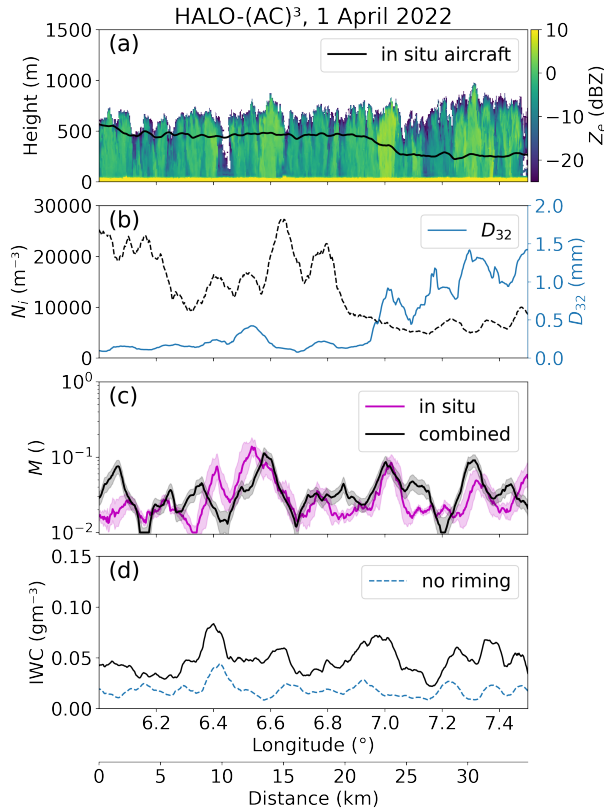


Figure 4. As in Fig. 3 but for the collocated flight segment from 1 April 2022 11:20:38-11:33:02 UTC during HALO-(AC)³. Only W-band radar reflectivities are available.

is negligible for HALO-(AC)³ due to the smaller particle sizes and $D_{32} < 3.2$ holds for 90% of the data. [In Appendix A](#), [Appendix A gives](#) an overview of microphysical parameters during each analyzed segment [is given](#).

370 4.2 Sensitivity study

To [motivate our further analysis](#) [show the effect of expected \$M\$ on \$Z_e\$](#) and to evaluate whether the retrieved amounts of riming significantly impact IWC, we conduct a sensitivity study.

We assume that $N(D_{\max})$ follows a modified gamma distribution and use the normalized form introduced by Delanoë et al. (2005, 2014) and extended by Maahn et al. (2015) for the maximum dimension D_{\max}

$$375 \quad N(D_{\max}) = N_0^* \frac{(b_m + \mu + 1)^{b_m + \mu + 1} \Gamma(b_m + 1)}{\Gamma(b_m + \mu + 1)(b_m + 1)^{b_m + 1}} \left(\frac{D_{\max}}{D_m} \right)^\mu e^{-(b_m + \mu + 1)D_{\max}/D_m}, \quad (7)$$

where N_0^* is the overall scaling parameter, μ [is](#) the shape parameter, and D_m is the "mass-weighted" scaling parameter for the particle size. We vary N_0^* and D_m —which can be calculated from PSD moments (see Maahn et al., 2015)—based on 10 to 90% quantile values derived from all measured PSDs during IMPACTS. [Exclusively IMPACTS data was](#) [Only IMPACTS](#)

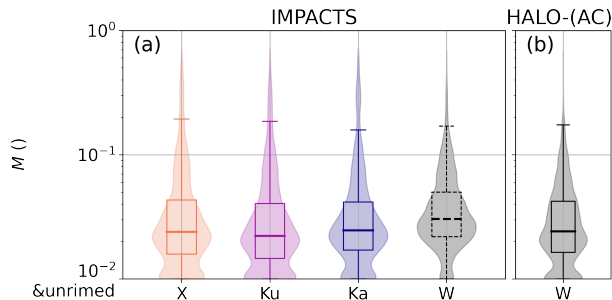


Figure 5. Box plots and superimposed violin plots showing normalized rime mass M results obtained from a closure of collocated radar reflectivity Z_e and in situ particle size distribution ("combined method" from Maherndl et al. (2024)) for radar reflectivities available during (a) IMPACTS and (b) HALO-(AC)³. W-band results during IMPACTS are dashed due to biases (see text). $M < 0.01$ are plotted at 0.01 to be visible on the logarithmic scale.

data were chosen, because larger particles and higher number concentrations were measured during IMPACTS than during HALO-(AC)³. μ is varied from 0 to 64 based on extreme values reported in the literature (Tridon et al., 2022). M is varied from 0.005 to 1, ~~which correspond~~ corresponding to the 10 % quantile of M retrieval results from both campaigns and the maximum "physical" M based on its definition.

We find that although the median M ~~are is~~ below 0.03 for both campaigns, even small amounts of riming—or rather changes in ice particle density—can result in large changes ~~of in~~ IWC. Figure 6 shows IWC calculations assuming gamma PSDs with varying N_0^* (left column) and M (right column) as a function of D_m . Similar to Maahn and Löhnert (2017), we find that the shape parameter μ does not significantly impact IWC or Z_e ~~significantly~~ and therefore only $\mu = 0$ is shown. D_m , which can be seen as a proxy for particle size, has the largest ~~impact effect~~ Changing D_m from 1 to 8 mm, ~~IWC changes~~ changes IWC by three orders of magnitude. IWC increases by about one order of magnitude, when N_0^* —the proxy for the total number concentration of particles—is increased by one order of magnitude. Depending on D_m , varying M can result in IWC changes of up to two ~~order of magnitudes. When only considering orders of magnitude. Considering only~~ M values encountered during the analyzed campaigns campaigns analyzed, the change in IWC reaches one order of magnitude.

~~To show the impact~~ In order to show the effect of riming on radar reflectivity Z_e , which can be ~~seen~~ considered as a proxy for IWC, we conduct a sensitivity study for ~~Ku-Ku-~~ and Ka-band Z_e . ~~In doing so, we aim~~ The aim is to highlight the importance of accounting for riming in radar retrievals. Z_e is forward simulated using the same PSDs with PAMTRA assuming a temperature of -10 °C. Particle scattering is parameterized with the riming-dependent parameterization (Maherndl et al., 2023a). X-band is not shown due to being nearly identical to Ku-band; W-band is not shown due to the riming-dependent parameterization bias for large D_m at W-band (see Sect. 4.1.3). Varying M within the observed ranges results in Z_e changes of up to 20 dB depending on D_m for both Ku- and Ka-band, ~~albeit with~~ although with a slightly larger spread at Ka-band. Similar to Fig. 6, varying D_m results in the largest Z_e changes. Observed ranges of M result in larger Z_e changes than observed ranges of N_0^* . ~~Therefore~~ Thus, in our data set, Z_e depends more ~~heavily~~ on riming than on number concentration.

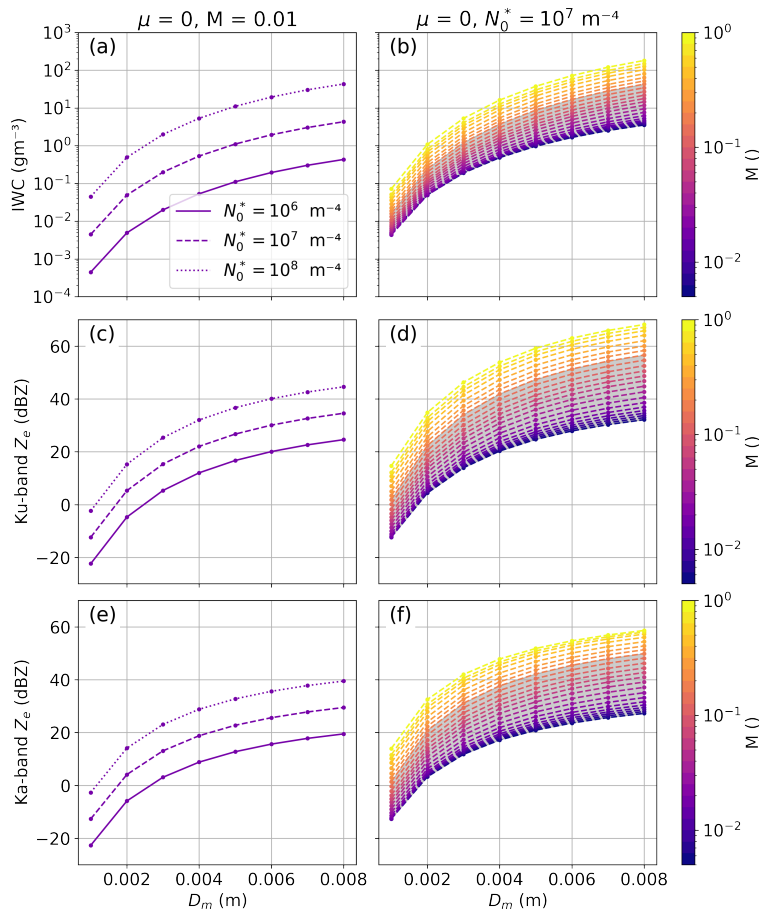


Figure 6. Ice water content (IWC) (top), Ku-band Z_e (middle), and Ka-band Z_e (bottom) calculated from gamma particle size distributions as functions of D_m parameter. Results for varying N_0^* parameter are shown as solid and dashed lines in (a), (c), (e); for varying normalized rime mass M are color-coded in (b), (d), (f). Shaded areas in (b), (d), (f), (h) indicate M ranges observed during IMPACTS (90 % range: $0.005 < M < 0.15$).

We therefore conclude that for the range of M observed during HALO-(AC)³ and IMPACTS, the effect of riming on IWC should not be neglected to avoid biases of up to one order of magnitude for in IWC.

4.3 Quantifying in-cloud IWC variability with and without riming

Because even small amounts of riming significantly impact IWC, we evaluate have a significant effect on IWC, in the following
 405 we evaluate the differences in IWC variability when accounting for riming vs. when neglecting riming in the following riming
is considered versus when riming is neglected. As described in Sect. 3.2, IWC is calculated with Eq. 4 based on the measured PSD and (1.) using mass-size parameters a_m and b_m for unrimed particles (IWC_u) and (2.) varying a_m and b_m for each time step as a function of the retrieved M (IWC_r). During all analyzed IMPACTS flight segments, the rime mass ($IWC_r - IWC_u$)

makes up 68.6 / 65.7 / 68.8 % of IWC_r , based on X- / Ku- / Ka-band results. During HALO-(AC)³, the rime mass makes up
410 62.7 %.

Figure 7 shows the average PCF η over all analyzed IMPACTS and HALO-(AC)³ segments for N_i (Fig. 7, first column), IWC_r , and IWC_u (Fig. 7, second column). To visualize the difference between IWC_r and IWC_u , Fig. 7, 3rd column shows the $\eta_{IWC_r} - \eta_{IWC_u}$. ~~By this, we can~~ This allows us to isolate the contribution of the riming process to IWC. Positive values of $\eta_{IWC_r} - \eta_{IWC_u}$ indicate that riming increases the variability of IWC clusters at the given lag, while negative values are related
415 to riming smoothing out IWC variability. Because we are interested at which spatial scales in the spatial scales at which riming influences IWC variability, we only discuss the differences larger-greater than zero.

~~Both in terms of~~ For both N_i and IWC, IMPACTS segments have higher η on average than HALO-(AC)³ segments meaning,
implying that N_i and IWC have more variability on the investigated spatial scales spatial scales examined (Fig. 7a, b). Note that
420 both quantities are calculated from running PSD averages of 10 s and 30 s for IMPACTS and HALO-(AC)³, respectively, to cover similar spatial scales (about 1.8 km) given the different flight speeds. The smaller count-number of data points averaged for IMPACTS might-could lead to higher variability. However, computing η for 30 s running averages results in similar curves with close-to-nearly the same lags where $\eta = 0$, and slightly lower η , yet-but still higher than for HALO-(AC)³ (not shown).

During IMPACTS, variability occurred at larger spatial scales than during HALO-(AC)³, as indicated by positive η at larger lags (Fig. 7a, b). Differences between η for N_i and IWC indicate that ice growth processes play a large role for-in IWC
425 variability in addition to ice formation processes. For both campaigns, $\eta > 0$ for IWC is shifted to larger spatial scales than for N_i , indicating, indicating that ice growth processes lead to increased variability at large spatial scales. For IMPACTS, accounting for riming shifts the scales of IWC variability to slightly smaller lags and increases η significantly at small lags, meaning-i.e. riming increases IWC variability at lags < 5 km (Fig. 7c). For HALO-(AC)³, riming leads to IWC variability at lags below 1 km as well as between 3-5 km. (Fig. 7c) However, the differences between η_{IWC_r} and η_{IWC_u} are smaller than
430 for IMPACTS.

4.3.1 Dependency on particle size

To identify which size-range-of-particles-particle size range contributes most to the N_i and IWC variability, we split the PSD into small ($50 < D_{max} < 300 \mu\text{m}$), medium ($300 < D_{max} < 900 \mu\text{m}$), and large ($D_{max} > 900 \mu\text{m}$) particle sizes to calculate N_i and IWC (Fig. 7d-i). For IMPACTS, the probability of small particle N_i (IWC) clusters is higher than for medium and large
435 particles below 3.5 km (10 km). During HALO-(AC)³, η is similar regardless of size. However, positive η_{IWC} —indicating the occurrence of IWC clusters—are clusters—are shifted to slightly larger lags for large particles (9 km as opposed to 5-6 km for small and medium sizes).

The measurement location in-cloud could influence the dependency-dependence of N_i and IWC variability on particle size due to size sorting, i.e. ~~r-~~ more small particles near the CTH and larger particles at lower heights. During the analyzed
440 HALO-(AC)³ segments, clouds were shallow and *Polar 6* measurements took place on average 440 m below the CTH (as measured by W-band radar). During IMPACTS, much deeper cloud systems were observed and *P-3* sampled on average in-at larger vertical distances from cloud top (3.3 km) than during HALO-(AC)³. W-band radar reflectivity Z_e —which can be seen

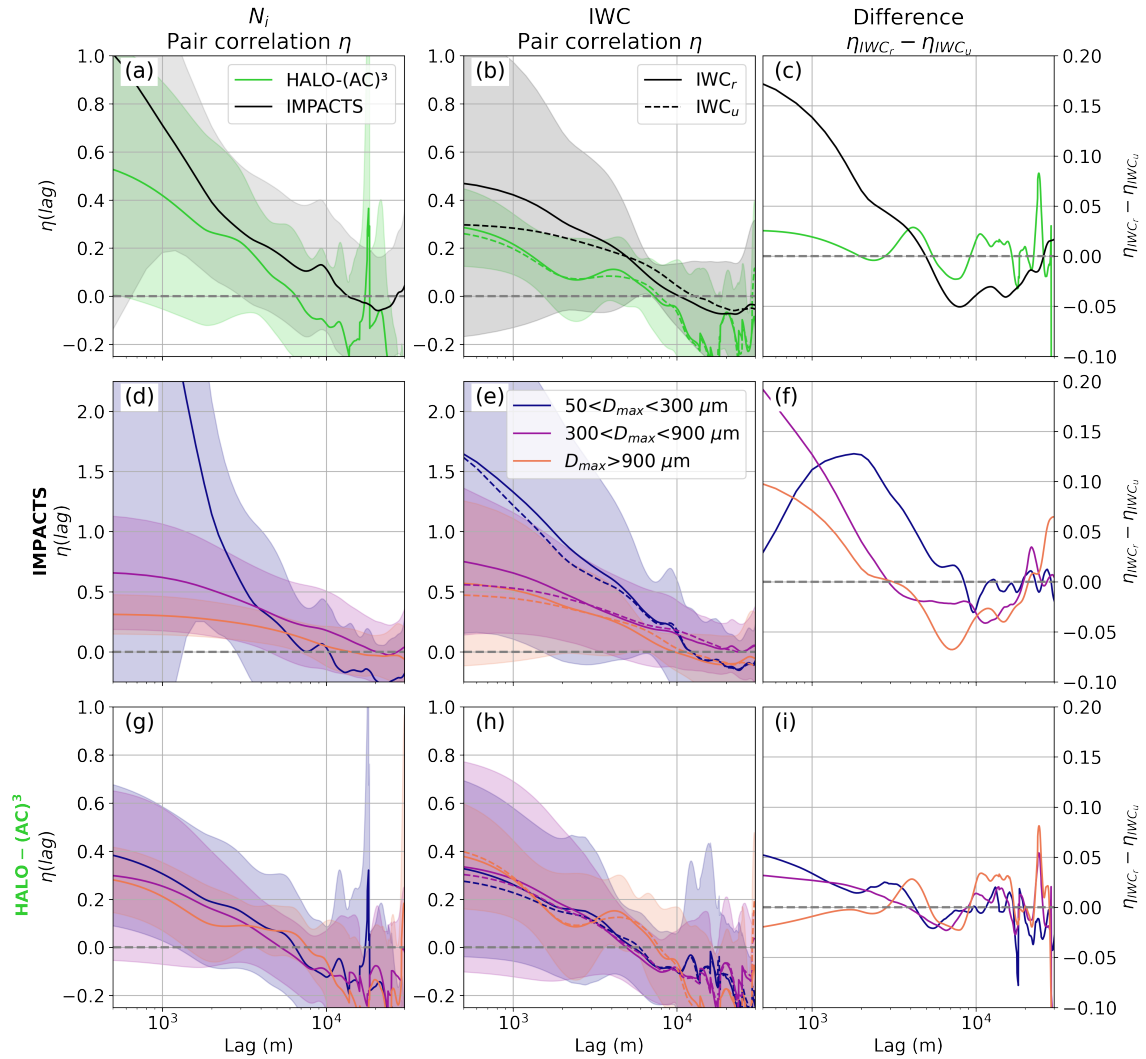


Figure 7. Average pair correlation function (PCF) η as a function of lag calculated for (a) ice number concentration N_i and (b) ice water content (IWC) during IMPACTS (black) and HALO-(AC)³ (green) segments. IWC is calculated with (solid line) and without (dashed line) accounting for riming and differences are plotted in (c). Shaded areas show standard deviations. In (d)-(i), the particle size distributions are split into small ($50 < D_{max} < 300 \mu\text{m}$), medium ($300 < D_{max} < 900 \mu\text{m}$), and large ($D_{max} > 900 \mu\text{m}$) particle sizes. (d)-(f) and (g)-(i) are as in (a)-(c) but showing size dependency of η during IMPACTS and HALO-(AC)³, respectively. Note the different y-axis scales.

as a proxy for IWC—shows higher variability close-to-near CTH for both IMPACTS and HALO-(AC)³ clouds (Fig. 8). Similar to Fig. 7, we use PCF to characterize the variability of Z_e in linear units. For each IMPACTS (HALO-(AC)³) flight segment, η is calculated for Z_e cross sections in 100 m (50 m) steps from the average CTH downward. In general, Z_e variability is larger close-to-cloud-top-near CTH at lags below 5 km and 2 km for IMPACTS and HALO-(AC)³, respectively. The higher variability is likely linked to cloud top generating cells, which-can-be-seen-e.g.,-as-seen in case study 1 (Fig. 3a). Generating cells contain

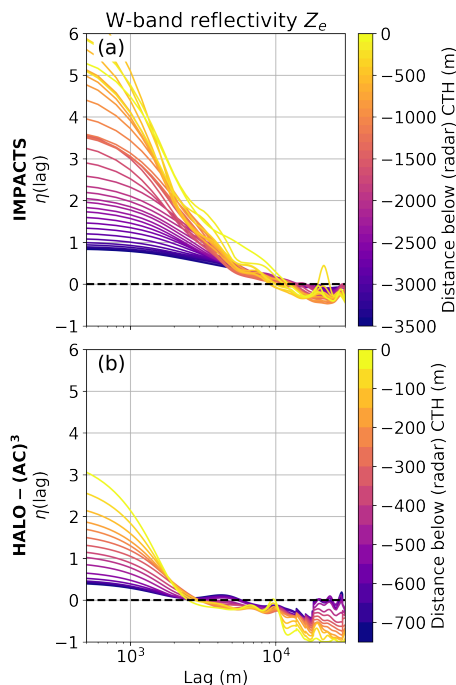


Figure 8. Average pair correlation function (PCF) η as a function of lag calculated for horizontal cross section of W-band Z_e (in linear units) during (a) IMPACTS and (b) HALO-(AC)³ flight segments. Cross sections are taken in 100 m and 50 m steps from the average cloud top height (CTH) of each segment downward for IMPACTS and HALO-(AC)³ data, respectively. Note the different colorbar scales.

more liquid and ice and have stronger updrafts than adjacent cloud regions. HALO-(AC)³ clouds show less variability and are homogeneous ~~on-at~~ smaller spatial scales ($\eta = 0$ is at smaller lags) than clouds during IMPACTS. Size sorting ~~might may~~ play a larger role for IMPACTS due to the larger cloud depths ~~as opposed compared~~ to the shallow MCAO clouds during HALO-(AC)³. However, ~~the~~ N_i and IWC distributions as functions of distance to CTH indicate the opposite (Appendix B). ~~Nonetheless~~ ~~Nevertheless~~, N_i and IWC derived for small particles only show much more variability ~~depending on as a function of~~ the distance to CTH for IMPACTS (Appendix B).

The higher variability of small particle counts during IMPACTS is therefore likely due to higher numbers of ice nucleating particles (INP) available at mid-latitudes (Petters and Wright, 2015). During the analyzed HALO-(AC)³ flight days, INP concentrations collected with filters on board of *Polar 6* were very low, ~~oftentimes often~~ below the detection threshold (Wendisch et al., 2024). No INP measurements were conducted during IMPACTS, therefore a direct comparison cannot be made. Another explanation could ~~possibly be be that~~ more secondary ice production (SIP) occurring during IMPACTS than during HALO-(AC)³.

Differences between η computed for IWC_r and IWC_u using the different size bins (Fig. 7f) show that riming ~~enhances increases~~ the probability of IWC clusters for lags smaller ~~than~~ 9 km for small particles during IMPACTS. For medium and large particles, riming ~~enhances IWC cluster probability increases the probability of IWC clusters~~ at lags smaller ~~than~~ 3 km.

~~The enhancement is larger the smaller the lag for~~ For medium and large particles, ~~whereas the enhancement increases as the lag decreases, while~~ for small particles ~~the largest enhancement is,~~ the maximum enhancement occurs at a lag of about 2 km. 465 An enhancement for small particles ~~possibly hints at SIP connected to riming~~ may indicate SIP associated with riming, such as rime splintering. During HALO-(AC)³ (Fig. 7i), riming enhances the probability of IWC clusters for lags smaller ~~than~~ 4 km for small and medium particles, and the enhancement is generally larger the smaller the lag. For large particles, only lags of about 3-5 km lead to an ~~enhancement of~~ increase in IWC variability.

4.3.2 Dependency on riming

470 To understand which spatial scales dominate the ~~riming driven~~ riming-driven IWC variability, we ~~conduct~~ perform a Monte-Carlo random test for specific sampling distances following Deng et al. (2024). This approach allows us ~~to first,~~ first, to handle the flight segments of different lengths in a statistically robust ~~way, and second,~~ manner and, second, to analyze the dependence on flight segment distance. For each flight segment, we randomly select a sub-segment with a distance of d km, where we vary d in 1 km steps from 1 to 15 km. Then, we calculate η for ~~this that~~ segment. This is repeated 100 times and the average η over 475 all (sub)segments of the respective campaign is calculated. ~~In principle, parts of sub-segments can be resampled. However, the sampling process is random.~~ To perform the averaging, we ~~bin-divide~~ η into 200 m and 60 m bins for IMPACTS and HALO-(AC)³, respectively, ~~which corresponds~~ corresponding to the respective distances covered in 1 s for the respective typical flight speeds. The results are shown in Fig. 9, where the average η for N_i , IWC_r , and IWC_u are plotted as ~~functions a function~~ of distance d and lag. Curves (shaded) where $\eta = 0$ are included to show the maximum spatial scales at which ice clusters ~~likely~~ 480 ~~are likely to~~ occur, given a sampling distance d .

During IMPACTS, the maximum N_i cluster spatial scale in clouds increases from 0.6 km to 3.1 km at distances d of 2 km to 15 km (Fig. 9a). ~~King probe-measured~~ LWC cluster scales ~~measured by the King probe~~ behave similarly to N_i (not shown) ~~and~~, ~~and the~~ maximum cluster scales increase from 0.6 km to 3.0 km. This suggests simultaneous liquid and ice formation in regions ~~with of~~ high supersaturation with respect to ice. Maximum IWC cluster scales (~~independent of accounting for riming~~ 485 ~~or not whether or not riming is considered~~) increase from 0.6 km to 3.6 km (Fig. 9b,c). At distances ~~smaller less than~~ 6 km, N_i and IWC have ~~about roughly~~ the same cluster scales; at distances ~~larger greater than~~ 10 km, IWC clusters occur at larger spatial scales. Differences between positive values of IWC_r and IWC_u (Fig. 9d) reveal that riming enhances the probability of ice clusters for distances ~~larger greater than~~ 6 km for lags from about 1 km to 10 km (at distances of 12 km). To show the statistical significance of this enhancement, a one-sided Student's t-test with a significance threshold of 95 % is used. Areas 490 where differences are significant are hatched (Fig. 9d). The enhancement occurs at similar spatial scales as LWC clusters, ~~indicating suggesting that~~ riming is driven by LWC variability.

During HALO-(AC)³, the maximum N_i cluster spatial scale in clouds increases from 0.5 km to 3.7 km at distances of 2 km to 15 km (Fig. 9e). Similar to IMPACTS data, ~~Nevzorov probe-measured LWC clusters behave similarly~~ LWC clusters ~~measured by the Nevzorov probe behave similarly to~~ N_i clusters, increasing from 0.5 km to 3.3 km, ~~however having but~~ 495 ~~with~~ slightly smaller spatial scales. Maximum IWC cluster scales, assuming no riming, increase from 0.6 km to 3.8 km and ~~therefore thus~~ occur at about the same spatial scales as N_i clusters (Fig. 9g). ~~When accounting~~ Accounting for riming, ~~the~~

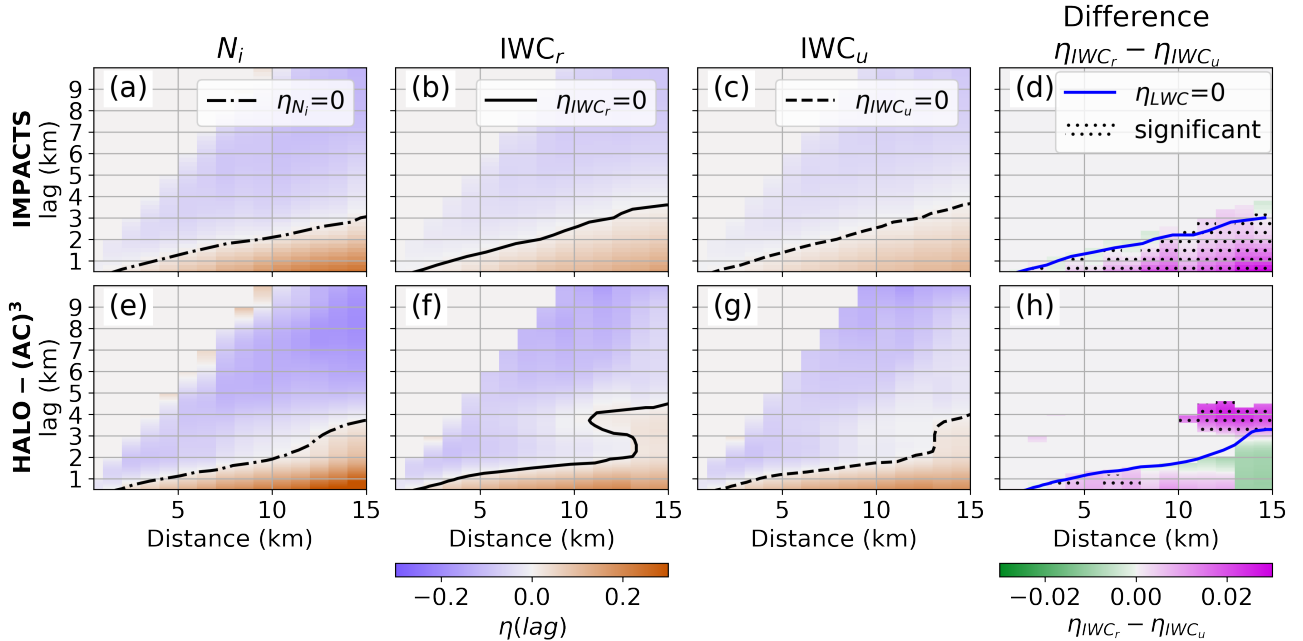


Figure 9. Average pair correlation function (PCF) η as a function of distance and lag calculated using all (a-c) IMPACTS and (e-g) HALO-(AC)³ flight segments for (a)&(e) N_i , (b)&(f) ice water content (IWC) accounting for riming IWC_r , and (c)&(g) IWC assuming no riming IWC_u . The Difference between (b) and (c) are shown in (d); difference between (f) and (g) in (h). Differences in (d) and (h) are only shown, where $\eta_{IWC_r} > 0$. Areas, where differences are significant according to a Student’s t-test (95 % significance threshold) are hatched. $\eta = 0$ is drawn as shaded lines for the ice number concentration N_i (dash-dotted black), IWC_r (solid black), IWC_u (dashed black), and liquid water content (LWC, solid blue), where LWC measurements from King probe (Nevzorov probe) measurements obtained during IMPACTS (HALO-(AC)³) are used.

maximum IWC cluster scales show a distinct behavior for distances larger than 10 km: η increases at 3-5 km indicating that riming ~~enhances variability on increases variability at~~ these scales (Fig. 9f), which cannot be explained by the LWC variability. Statistically significant differences between positive IWC_r and IWC_u (Fig. 9h), further highlight this feature.

500 To explain the different spatial scales ~~where riming enhances at which riming increases~~ IWC variability, we look at ~~lidar derived lidar-derived~~ CTH. In previous sections, we derived CTH from radar measurements to make IMPACTS and HALO-(AC)³ comparable. ~~During For~~ HALO-(AC)³, a more sophisticated CTH product based on lidar—which is more sensitive to liquid layers at cloud top than the radar—is available and ~~used the following, is used below~~. The lidar detects small liquid droplets at cloud top, which follow vertical motions, therefore leading to higher CTH in updraft regions (Abel et al., 2017).
 505 When computing the average power spectrum of CTH observed during the ~~studied flight days flight days studied~~, distinct peaks at wavelengths of 750 m and 1.2 km occur for all days, ~~which corresponds~~. ~~These wavelengths correspond~~ to the typical roll cloud and circulation wavelengths as derived by Schirmacher, et al. (2024) (Fig. 10a, d, g). At these wavelengths, peaks in LWP also occur for all days (Fig. 10b, e, h), further indicating enhanced formation and growth of liquid droplets in the

updraft regions of the convective cell cloud structures. On 28 March, a ~~distinctive prominent~~ peak in the CTH spectrum at 510 3-5 km indicates additional mesoscale updraft features (Fig. 10a). However, the LWP spectrum ~~only shows~~ shows only a weak peak ~~towards around~~ 5 km (Fig. 10b). On 1 April, both CTH and LWP power spectra have peaks at 3-5 km (Fig. 10d,e). On 4 April, ~~no peak distinctive there are no prominent~~ peaks at wavelengths of 3-5 km ~~are visible~~ (Fig. 10g,h). Given that the least (most) amount of riming (Fig. 10c,f,i) occurred on 4 (1) April, we conclude that in the studied MCAO clouds, mesoscale updraft features likely enhance riming at spatial scales of 3-5 km. The enhancement could ~~occur either due to~~ be due to either 515 prolonged lifetimes of ice crystals in clouds (28 March) or increased amounts of liquid water or both (01 April), and leads to an increase in IWC amount and variability.

4.4 A conceptual model of how riming impacts IWC clusters in MCAO roll clouds

The results discussed above help to better understand scales of in-cloud IWC clustering in different types of ~~MPC and link~~ to some MPCs and link them to some of the microphysical processes involved. Although there are ~~substantial significant~~ 520 unknowns, the following summarizes our findings from the perspective of collocated remote sensing and in situ measurements.

In the analyzed segments of winter storm clouds measured during IMPACTS, IWC clusters occur at spatial scales smaller than about 3 km for segment distances of 15 km. Accounting for riming ~~enhances ice cluster probabilities~~ increases the probability of ice clusters (Fig. 9d). However, riming does not ~~lead to significantly enhanced~~ significantly increase the occurrences of IWC clusters at ~~other specific~~ scales. LWC clusters for segment distances of 15 km occur at the same spatial scales 525 of about 3 km as clusters of N_i . Therefore, liquid droplets and ice particles are likely ~~formed to form~~ together in regions ~~with of~~ supersaturation with respect to liquid and ice. ~~Because Since~~ LWC clusters and the IWC cluster enhancement ~~through by~~ riming occur at similar spatial scales, we hypothesize that LWC variability (at least in part) drives riming. By increasing IWC, riming leads to ~~enhanced increased~~ probabilities of IWC clusters for IMPACTS.

For HALO-(AC)³, Fig. 11 shows a sketch of the maximum spatial scales, where we found ice clusters to occur for MPCs 530 observed during MCAOs. In these MCAO roll clouds, ice clusters occur ~~at on~~ spatial scales of the roll cloud wavelengths. In the updraft regions of the ~~convective convective~~ cells, which occurred on average every 750 m and 1.2 km, liquid droplets and ice particles are formed. LWP and CTH are increased ~~due to the by~~ vertical motions and ~~liquid condensation~~ condensational growth. Ice particles grow through depositional growth and riming, ~~which leads leading~~ to enhanced probabilities of ice clusters at these scales. When ~~ice particles' masses have an ice particle's mass has~~ increased sufficiently, ~~they precipitate or might it~~ 535 may precipitate or sublimate below cloud. Aggregation ~~might occur as can occur when~~ ice particles collide. In the presence of additional mesoscale updraft features, IWC clusters also occur at spatial scales of 3-5 km (Fig. 9h). Due to the ~~stronger~~ increased vertical motion, ice particles are suspended longer, have more time to rime, and can reach higher masses before precipitating. Increased LWP ~~might may~~ enhance the amount of riming, but is not a necessary criterion based on the ~~analyzed~~ eases cases analyzed. This hypothesis is supported by the fact that the observed LWP is not sufficient to explain the retrieved 540 rime masses ~~assuming particles continuously collecting~~, assuming that particles continuously collect liquid water by falling through the liquid layer, as we show in Appendix C. The enhanced occurrence of riming drives the additional increase ~~of in~~ IWC cluster probability ~~at on~~ spatial scales of 3-5 km.

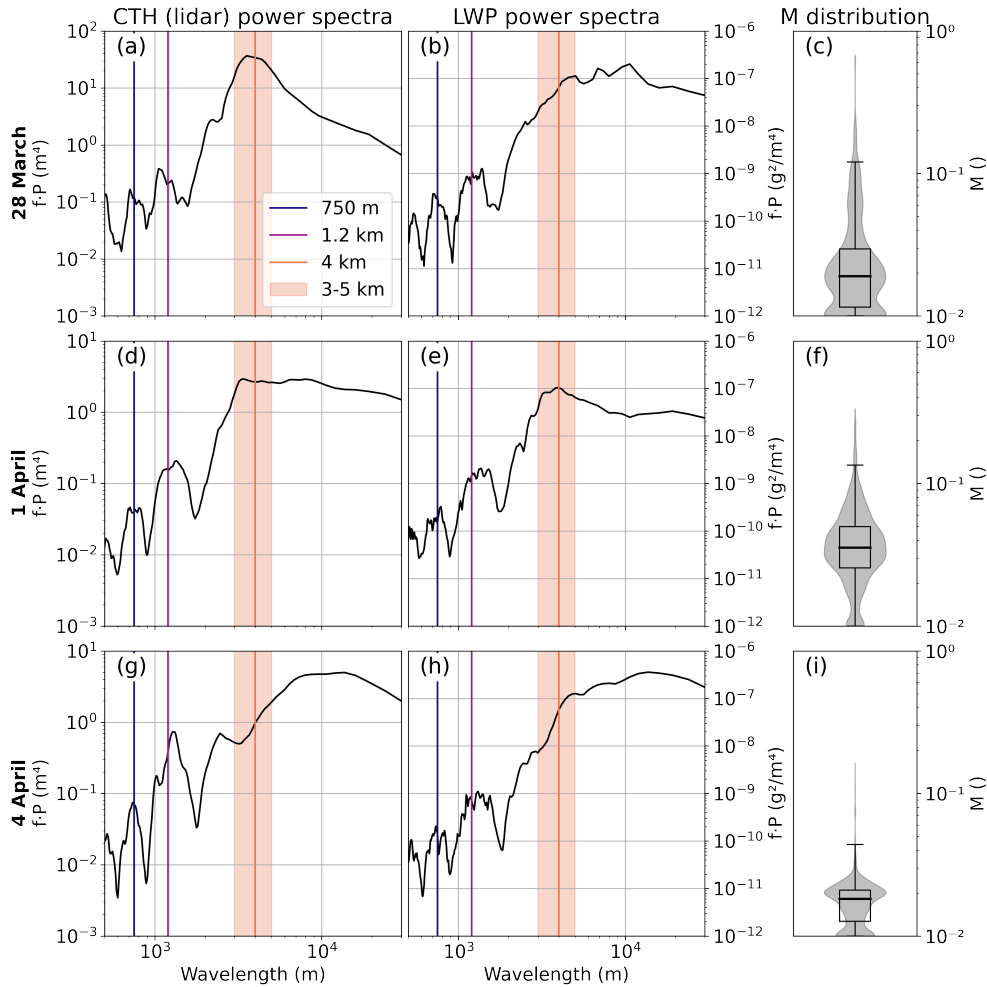


Figure 10. Power spectra of (a), (d), and (g) cloud top height (CTH) as derived from lidar and (b), (e), and (h) liquid water path (LWP) during collocated HALO-(AC)³ flight days. The wavelength has been calculated based on the aircraft flight speed. The blue and purple lines show the typical roll cloud and circulation wavelengths as derived by Schirmacher, et al. (2024). The orange shaded area shows the 3-5 km range, where riming causes additional IWC clustering. (c), (f), and (i) show the corresponding normalized rime mass M distributions.

5 Conclusions

In this study, we use airborne measurements of mid- and high-latitude mixed-phase clouds (MPC) in mid- and high-latitudes ~~are used to study MPCs~~ to investigate the spatial variability of ice clusters within clouds. We further investigate how this variability is linked to riming, which we quantify by through the closure of collocated cloud radar reflectivity and in situ particle size distribution (PSD) measurements. ~~Pair~~ The pair correlation function (PCF) is used to quantify ice cluster scales ~~and the spatial scales of ice clusters and the variability of~~ ice water content (IWC) variability when first, when accounting for riming (IWC_r) ~~and second, and~~ neglecting riming (IWC_u). The main findings are as follows:

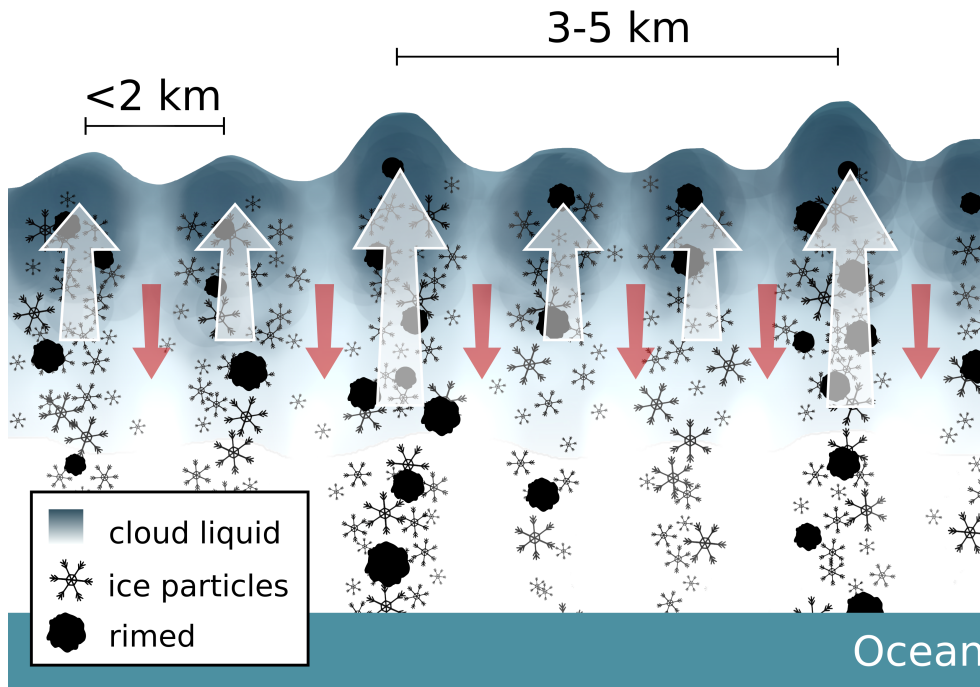


Figure 11. A conceptual diagram summarizing ice cluster spatial scales driven by riming as observed in MCAO roll clouds during HALO-(AC)³. For further explanations see text.

- 550 1. Although the synoptic situations and the resulting clouds-cloud systems were vastly different during the two analyzed aircraft campaigns aircraft campaigns analyzed, the retrieved amounts of riming were similar with. The median normalized rime masses-mass M of was 0.023 and 0.024 during IMPACTS (mid-latitude winter storms) and HALO-(AC)³ (Arctic MCAO roll clouds) segments, respectively (Fig. 5). Clouds were deep (shallow) during IMPACTS (HALO-(AC)³) segments, and in situ measurements were conducted on-average-in-vertical-distances-at-an-average vertical distance of
- 555 3.3 km (440 m) from cloud top.
2. The observed spread of M can increase IWC by up to two orders of magnitude, depending on the size of the particle population (Fig. 6). In sum, the rime mass makes up about 66 % and 63 % of the total IWC during the analyzed IMPACTS and HALO-(AC)³ flight segments, respectively. Therefore, riming has a similar impact on IWC as the observed spread of number concentration and should not be neglected when estimating IWC.
- 560 3. PCF revealed that N_i cluster-clusters occur with increased probability on-at spatial scales smaller than 10.5 km and 6.5 km within clouds during IMPACTS and HALO-(AC)³, respectively. IWC clusters dominate for spatial scales of 10 km and 7 km. During-For IMPACTS, small particles dominate N_i and IWC variability on small spatial scales, whereas while for HALO-(AC) there is no dependence-on-particle-size-during-HALO-(AC)³-(particle size dependence (Fig. 7).

This could be ~~linked-related~~ to ice formation processes and the higher availability of INP at mid-latitudes. However, this hypothesis could not be confirmed with the available data.

565

4. During IMPACTS, ~~maximum the maximum spatial scales of N_i , IWC and LWC cluster spatial scales, and LWC clusters~~ inside clouds are 0.6-3 km for distances of 2-15 km ~~and increase to about 3 for distances of 15~~. During HALO-(AC)³, ~~maximum the maximum spatial scales of N_i , IWC and LWC cluster spatial scales, and LWC clusters~~ are similar with about 0.5 km for distances of 2 km and about 4 km for 15 km. However, ~~for IWC during HALO-(AC)³ IWC cluster probability, the probability of cluster occurrence~~ is increased on scales of 3-5 km when segment distances are larger ~~than~~ 10 km (Fig. 9).

570

5. During IMPACTS, accounting for riming does not significantly change IWC cluster scales in clouds, but increases the probability of clusters for segment distances larger than 6 km (Fig. 9d). This enhancement occurs at ~~similar scales as scales similar to~~ LWC variability. More riming ~~likely occurs in regions with enhanced concentration of liquid water and increases is likely to occur in regions of enhanced LWC, increasing~~ IWC. Since clusters of IWC neglecting riming have similar spatial scales as N_i , LWC, and IWC accounting for riming, ice clustering is likely linked to ice formation processes in regions of high supersaturation with respect to liquid and ice.

575

6. In contrast, riming impacts IWC clustering in clouds at two ~~distinctive-distinct~~ scales during HALO-(AC)³ (Fig. 9h). First, riming ~~enhances-increases~~ the probability of IWC clusters at spatial scales below 2 km, which corresponds to the wavelength of the roll cloud updraft features. N_i , IWC_r, IWC_u, and LWC all have similar spatial variability, indicating simultaneous ice and liquid formation and growth in ~~this regions. The enhanced concentrations of liquid again enhance these regions. Increased LWC again increase~~ riming, which increases IWC. Second, riming leads to IWC clustering ~~at on~~ spatial scales of 3-5 km, which cannot be explained by the typical roll cloud and roll circulation wavelengths. Power spectra of CTH show peaks at these spatial scales on the flight days with enhanced riming (Fig. 10). This ~~indicates suggests~~ that the presence of mesoscale updraft features—which cause ~~higher-greater CTH through~~ lifting of small particles near cloud ~~top and therefore increased CTH—leads top—leads~~ to enhanced occurrence of riming and ~~therefore hence~~ additional IWC clustering. Increased LWP ~~might increase may enhance~~ the effect, but is not a necessary criterion based on the ~~analyzed dayscases analyzed~~. Theoretical analysis shows that updrafts are likely ~~required-necessary~~ to explain the observed riming values (Fig. C1).

580

585

590 These results help to improve our understanding of how riming is linked to in-cloud IWC variability and can be used to evaluate and constrain ~~MPC-models~~ ~~models' representations of MPCs~~. While we have shown that riming enhances in-cloud IWC variability and causes additional IWC clustering at large spatial scales of 3-5 km in Arctic MCAO clouds, further research is needed to link these ~~findings-results~~ to surface precipitation. Future studies should investigate the link between riming-driven IWC variability and snowfall variability. In addition, profiles of vertical wind speed and turbulence are needed to better understand their importance for riming.

595

Data availability. Processed in situ (<https://doi.org/10.1594/PANGAEA.963247>, Moser et al., 2023), Nevzorov probe (<https://doi.org/10.1594/PANGAEA.963628>, Lucke et al., 2024) and MiRAC-A data (<https://doi.org/10.1594/PANGAEA.964977>, Mech et al., 2024a) as well as AMALi CTH (<https://doi.org/10.1594/PANGAEA.96498>, Mech et al., 2024b) from the HALO-(AC)³ campaign are available on PANGAEA. The IMPACTS data (<https://doi.org/10.5067/IMPACTS/DATA101>, McMurdie et al., 2019) and the individual datasets cited within this paper can be found at the NASA Global Hydrology Resource Center's DAAC. The data set of simulated rimed aggregates generated for Maherndl et al. (2023a) is available at <https://doi.org/10.5281/zenodo.7757034> (Maherndl et al., 2023b). HALO-(AC)³ datasets used in this study can be accessed via the ac3airborne intake catalog (<https://doi.org/10.5281/zenodo.7305585>, Mech et al., 2022b). Processing routines to read IMPACTS data are available via the `impacts_tools` repository (https://github.com/joefinlon/impacts_tools).

Appendix A: Microphysical overview of analyzed segments

605 Figure A1 (A2) presents an overview of microphysical parameters (N_i , D_{32} , M , IWC, LWC) observed during each analyzed IMPACTS (HALO-(AC)³) segment. Case study 1 (case study 2) is the fifth segment on 5 February (second segment on 1 April).

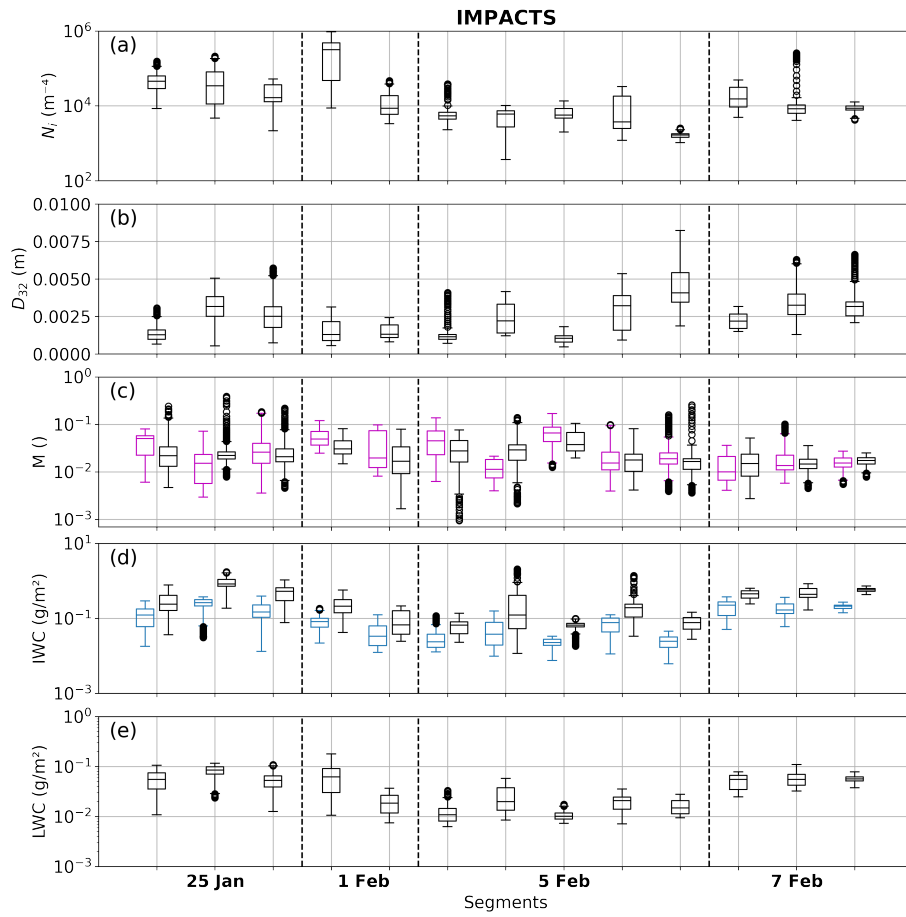


Figure A1. Boxplots of (a) ice number concentration N_i , (b) mass-weighted diameter D_{32} , (c) normalized rime mass M , (d) ice water content (IWC), and (e) liquid water content (LWC) derived during each IMPACTS segment. In (c) both combined (Ku-band) and in situ method results are shown in black and magenta, respectively. In (d) IWC is calculated accounting for riming (using combined method M ; black) and neglecting riming ($M = 0$, blue).

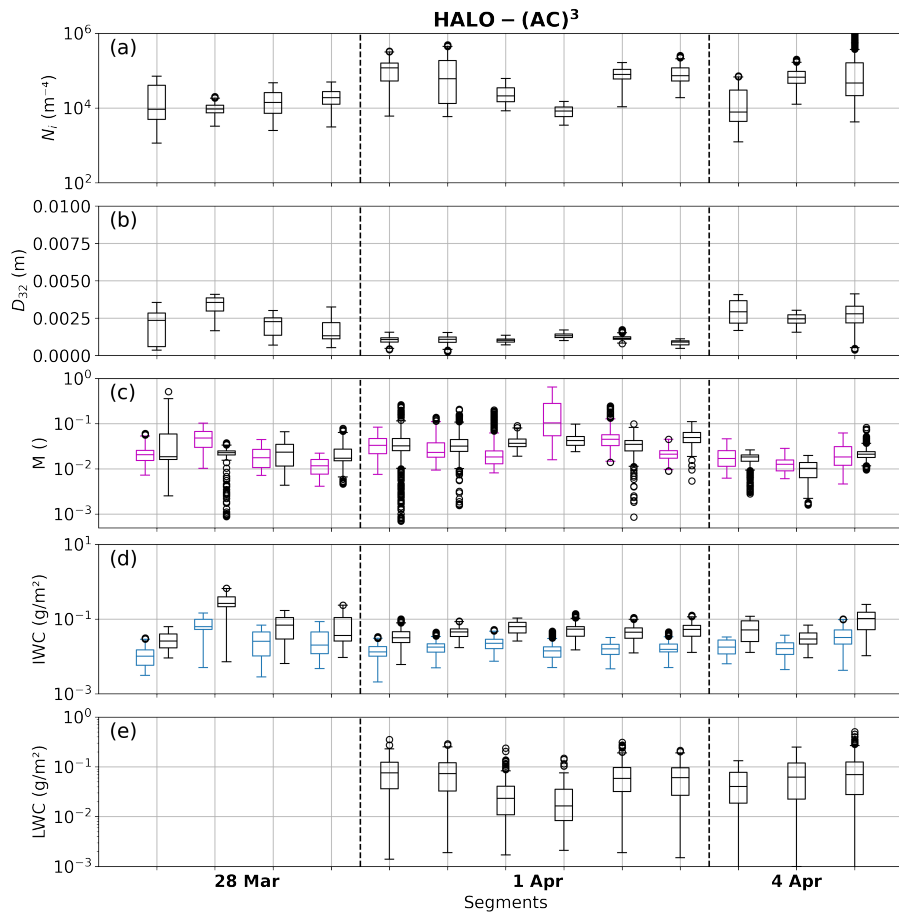


Figure A2. As in Fig. A1 but for HALO-(AC)³ segments

Appendix B: Vertical distribution of N_i and IWC

To investigate whether size sorting is the reason ~~of for~~ the particle size ~~dependency-dependence~~ of N_i and IWC variability
610 (Sect. 4.3.1), we show vertical distributions of N_i and IWC for the different size ranges in Fig. B1 and Fig. B2, respectively.
Data during collocated segments ~~is-are~~ binned by their distance to CTH (as derived ~~by from~~ radar measurements) in 100 m
bins. Only bins with ~~minimum-at least~~ 100 data points are shown. This leaves no data for 1.5 km below cloud top during
IMPACTS. While HALO-(AC)³ data ~~shows size sorting close to show size sorting near the~~ cloud top for both N_i and IWC,
this is not the case for IMPACTS. However, size sorting could have ~~happened-occurred~~ in the vertical region where we lack
615 data. ~~Nonetheless~~ Nevertheless, N_i and IWC for small particles show much larger variability during IMPACTS than during
HALO-(AC)³ ~~regardless of, regardless of the~~ distance to cloud top.

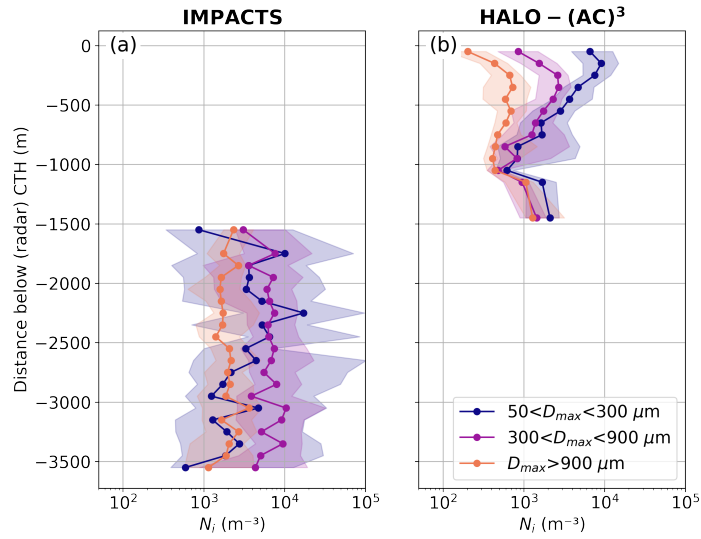


Figure B1. Distribution of ice number concentration N_i as a function of distance to cloud top height (CTH, derived by radar) for (a) IMPACTS and (b) HALO-(AC)³. Lines and markers show median values; 25-75 % quantiles are shaded. Contributions of small ($50\text{-}300 \mu\text{m}$), medium ($300\text{-}900 \mu\text{m}$), and large ($>900 \mu\text{m}$) particles are shown in blue, purple, and orange.

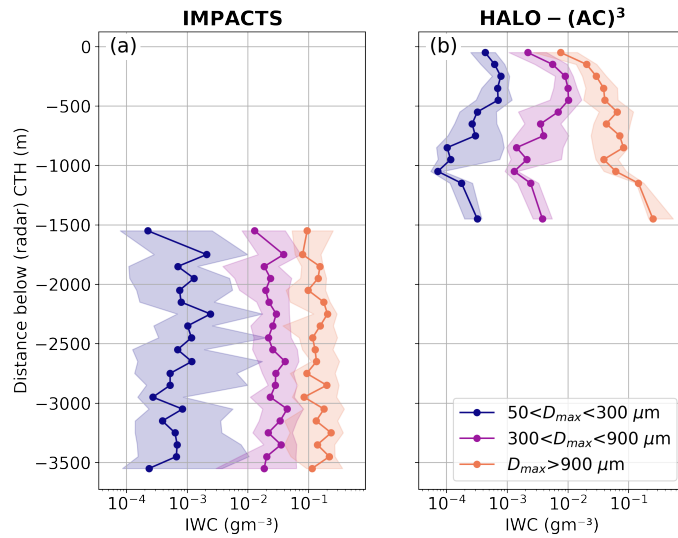


Figure B2. As in Fig. B1 but for ice water content (IWC; calculated accounting for riming).

Appendix C: LWP riming calculations

This section shows the need for updrafts to explain the retrieved amounts of riming given the observed LWPs. We use simple calculations based on Fitch and Garrett (2022). Assuming [that](#) a particle collects rime by falling through a liquid layer, the mass of rime accumulated can be approximated by

$$m_{rime} = A_p E_c \text{LWP}, \quad (\text{C1})$$

where A_p is the cross-sectional area of the particle, E_c is the combined collection and collision efficiency, and LWP is the liquid water path of the liquid layer. By inserting the definition of M , approximating A_p by a power law function of D_{max} with prefactor a_A and exponent b_A following Mahernndl et al. (2023a), and solving for LWP, we derive

$$\text{LWP} = \frac{M m_g}{A_p} = \frac{\pi \rho_g M}{6 a_A(M)} D_{max}^{3-b_A(M)}. \quad (\text{C2})$$

Here, E_c is assumed to be 1 as a worst case estimate, although [in the Arctic](#) lower values are more realistic [in the Arctic](#) (Fitch and Garrett, 2022). Eq. C2 [only holds-applies only](#) for ice particles that have finished the riming process. It is therefore only applied to HALO-(AC)³ data, where LWC=0 was measured, [thereby we exclude thus excluding](#) 28 March data, where LWC measurements are not available. Because ice particles occur in PSDs, we apply Eq. C2 to D_{32} as a proxy for the characteristic size and the respective M we retrieved for each time step. Compared to LWP observations during 1 and 4 April, the calculated LWP is much higher (Fig. C1). Therefore, it is evident [that](#) the particles must have been exposed to the liquid layer multiple times, e.g. [by](#) cycling through up- and downdraft regions.

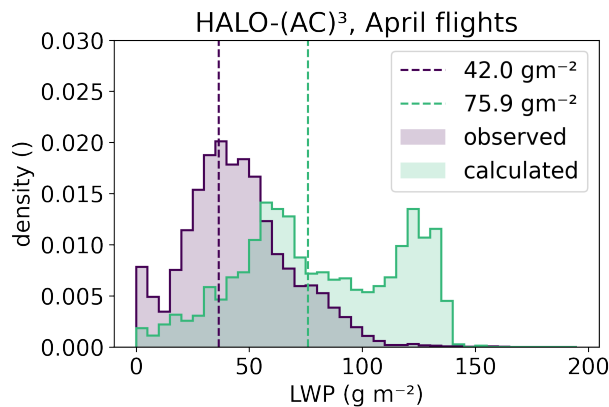


Figure C1. Normalized histograms of observed and calculated liquid water path (LWP) including medians (dashed lines). Observed LWP are from all 1 and 4 April data points. Calculated LWP were only derived for time steps where LWC=0, such that it can be assumed that no further riming will take place.

Author contributions. NM conceptualized the study, analyzed and plotted the data, and wrote the paper. MMA contributed to the concept, acquired funding, and supervised the research project. MMo and CV collected and processed CDP, CIP, and PIP data during HALO-(AC)³ and provided combined size distributions. JL collected and processed Nevzorov probe data during HALO-(AC)³. IS collected and processed AMALi data during HALO-(AC)³ and retrieved the CTH product. AB collected and processed CDP, Fast-CDP, 2D-S, and HVPS-3 data during IMPACTS and provided combined size distributions. All authors reviewed and edited the draft.

Competing interests. The authors declare no competing interests.

Acknowledgements. We gratefully acknowledge funding from the Deutsche Forschungsgemeinschaft (DFG, German Research Foundation) within the framework of the Transregional Collaborative Research Center “Arctic Amplification: Climate Relevant Atmospheric and Surface Processes, and Feedback Mechanisms” project ((AC)3; grant no. 268020496–TRR 172).

Sea ice concentration data from 20 March to 10 April 2022 were obtained from <https://www.meereisportal.de> (last access: 2 June 2023) (grant no. REKLIM-2013-04).

We thank Mario Mech and Nils Risse from the University of Cologne for providing processed MiRAC-A and AMALi data (together with IS) as well as the retrieved LWP product during HALO-(AC)³. Further, we thank Christof Lüpkes and Jörg Hartmann from the Alfred Wegener Institute (AWI) for providing Polar 6 noseboom air temperature measurements. We also thank Gerald M. Heymsfield, Matthew Walker McLinden, and Li Lihua from the NASA Goddard Space Flight Center for providing EXRAD, HIWRAP, and CRS data during IMPACTS. We are grateful to Joseph A. Finlon from the University of Washington for providing processing routines for the IMPACTS data. Further, we would like to acknowledge discussions with Matthew D. Shupe (University of Colorado and National Oceanographic and Atmospheric Administration), Heike Kalesse-Los (Leipzig University), and Patric Seifert (Leibniz Institute for Tropospheric Research) among others, whose feedback helped to shape the analysis.

References

- NASA Worldview, MODIS level-2 cloud product, <https://worldview.earthdata.nasa.gov>.
- 655 Abel, S. J., Boutle, I. A., Waite, K., Fox, S., Brown, P. R. A., Cotton, R., Lloyd, G., Choulaton, T. W., and Bower, K. N.: The Role of Precipitation in Controlling the Transition from Stratocumulus to Cumulus Clouds in a Northern Hemisphere Cold-Air Outbreak, *Journal of the Atmospheric Sciences*, 74, 2293 – 2314, <https://doi.org/10.1175/JAS-D-16-0362.1>, <https://journals.ametsoc.org/view/journals/atsc/74/7/jas-d-16-0362.1.xml>, 2017.
- Baker, B. and Lawson, R. P.: Analysis of Tools Used to Quantify Droplet Clustering in Clouds, *Journal of the Atmospheric Sciences*, 67, 3355–3367, ISSN 0022-4928, 1520-0469, <https://doi.org/10.1175/2010JAS3409.1>, 2010.
- 660 Bansemer, A., Delene, D., Heymsfield, A. J., O'Brien, J., Poellot, M. R., Sand, K., Sova, G., Moore, J., and Nairy, C.: NCAR Particle Probes IMPACTS.Dataset available online from the NASA Global Hydrometeorology Resource Center DAAC, Huntsville, Alabama, U.S.A. , <https://doi.org/10.5067/IMPACTS/PROBES/DATA101>, <http://dx.doi.org/10.5067/IMPACTS/PROBES/DATA101>, 2022.
- Baumgardner, D., Jonsson, H., Dawson, W., O'Connor, D., and Newton, R.: The Cloud, Aerosol and Precipitation Spectrometer: A New Instrument for Cloud Investigations, *Atmospheric Research*, 59–60, 251–264, ISSN 0169-8095, [https://doi.org/10.1016/S0169-8095\(01\)00119-3](https://doi.org/10.1016/S0169-8095(01)00119-3), 2001.
- 665 Baumgardner, D., Abel, S. J., Axisa, D., Cotton, R., Crosier, J., Field, P., Gurganus, C., Heymsfield, A., Korolev, A., Krämer, M., Lawson, P., McFarquhar, G., Ulanowski, Z., and Um, J.: Cloud Ice Properties: In Situ Measurement Challenges, *Meteorological Monographs*, 58, 9.1–9.23, <https://doi.org/10.1175/AMSMONOGRAPHIS-D-16-0011.1>, 2017.
- Bjardal, J., Storelvmo, T., Alterskjær, K., and Carlsen, T.: Equilibrium Climate Sensitivity above 5 °C Plausible Due to State-Dependent Cloud Feedback, *Nature Geoscience*, 13, 718–721, ISSN 1752-0908, <https://doi.org/10.1038/s41561-020-00649-1>, 2020.
- 670 Bock, J., Michou, M., Nabat, P., Abe, M., Mulcahy, J. P., Ollivier, D. J. L., Schwinger, J., Suntharalingam, P., Tjiputra, J., van Hulten, M., Watanabe, M., Yool, A., and Séférian, R.: Evaluation of Ocean Dimethylsulfide Concentration and Emission in CMIP6 Models, *Biogeosciences*, 18, 3823–3860, ISSN 1726-4170, <https://doi.org/10.5194/bg-18-3823-2021>, 2021.
- Cao, Q., Huang, Y., Zou, J., Lin, W., Zhou, X., Li, H., and Zhang, X.: Predicted Particle Properties (P3) Microphysics Scheme Coupled With WRF-Chem Model: Evaluation With Convective and Stratiform Cases, *Journal of Geophysical Research: Atmospheres*, 128, e2022JD037685, <https://doi.org/https://doi.org/10.1029/2022JD037685>, <https://agupubs.onlinelibrary.wiley.com/doi/abs/10.1029/2022JD037685>, e2022JD037685 2022JD037685, 2023.
- 675 Chase, R. J., Finlon, J. A., Borque, P., McFarquhar, G. M., Nesbitt, S. W., Tanelli, S., Sy, O. O., Durden, S. L., and Poellot, M. R.: Evaluation of Triple-Frequency Radar Retrieval of Snowfall Properties Using Coincident Airborne In Situ Observations During OLYMPEX, *Geophysical Research Letters*, 45, 5752–5760, ISSN 1944-8007, <https://doi.org/10.1029/2018GL077997>, <https://onlinelibrary.wiley.com/doi/abs/10.1029/2018GL077997>, 2018.
- 680 Choi, Y.-S., Ho, C.-H., Park, C.-E., Storelvmo, T., and Tan, I.: Influence of Cloud Phase Composition on Climate Feedbacks, *Journal of Geophysical Research: Atmospheres*, 119, 3687–3700, ISSN 2169-8996, <https://doi.org/10.1002/2013JD020582>, 2014.
- Connelly, R. and Colle, B. A.: Validation of Snow Multibands in the Comma Head of an Extratropical Cyclone Using a 40-Member Ensemble, *Weather and Forecasting*, 34, 1343–1363, ISSN 1520-0434, 0882-8156, <https://doi.org/10.1175/WAF-D-18-0182.1>, 2019.
- 685 Delanoë, J., Protat, A., Testud, J., Bouniol, D., Heymsfield, A. J., Bansemer, A., Brown, P. R. A., and Forbes, R. M.: Statistical Properties of the Normalized Ice Particle Size Distribution, *Journal of Geophysical Research: Atmospheres*, 110, ISSN 2156-2202, <https://doi.org/10.1029/2004JD005405>, 2005.

- Delanoë, J. M. E., Heymsfield, A. J., Protat, A., Bansemer, A., and Hogan, R. J.: Normalized Particle Size Distribution for Remote Sensing Application, *Journal of Geophysical Research: Atmospheres*, 119, 4204–4227, ISSN 2169-8996, <https://doi.org/10.1002/2013JD020700>, 2014.
- Deng, Y., Yang, J., Yin, Y., Cui, S., Zhang, B., Bao, X., Chen, B., Li, J., Gao, W., and Jing, X.: Quantifying the Spatial Inhomogeneity of Ice Concentration in Mixed-Phase Stratiform Cloud Using Airborne Observation, *Atmospheric Research*, 298, 107 153, ISSN 0169-8095, <https://doi.org/10.1016/j.atmosres.2023.107153>, 2024.
- 695 Erfani, E. and Mitchell, D. L.: Growth of Ice Particle Mass and Projected Area during Riming, *Atmospheric Chemistry and Physics*, 17, 1241–1257, ISSN 1680-7316, <https://doi.org/10.5194/acp-17-1241-2017>, 2017.
- Field, P. R., Hogan, R. J., Brown, P. R. A., Illingworth, A. J., Choularton, T. W., Kaye, P. H., Hirst, E., and Greenaway, R.: Simultaneous Radar and Aircraft Observations of Mixed-Phase Cloud at the 100 m Scale, *Quarterly Journal of the Royal Meteorological Society*, 130, 1877–1904, ISSN 1477-870X, <https://doi.org/10.1256/qj.03.102>, 2004.
- 700 Finlon, J. A., McMurdie, L. A., and Chase, R. J.: Investigation of Microphysical Properties within Regions of Enhanced Dual-Frequency Ratio during the IMPACTS Field Campaign, *Journal of the Atmospheric Sciences*, 79, 2773–2795, ISSN 0022-4928, 1520-0469, <https://doi.org/10.1175/JAS-D-21-0311.1>, 2022.
- Fitch, K. E. and Garrett, T. J.: Graupel Precipitating From Thin Arctic Clouds With Liquid Water Paths Less Than 50 g M⁻², *Geophysical Research Letters*, 49, e2021GL094 075, ISSN 1944-8007, <https://doi.org/10.1029/2021GL094075>, 2022.
- 705 Harimaya, T. and Sato, M.: Measurement of the Riming Amount on Snowflakes, *Journal of the Faculty of Science, Hokkaido University*, 8, 355–366, 1989.
- Heymsfield, A. J.: A Comparative Study of the Rates of Development of Potential Graupel and Hail Embryos in High Plains Storms, *Journal of the Atmospheric Sciences*, 39, 2867–2897, ISSN 0022-4928, 1520-0469, [https://doi.org/10.1175/1520-0469\(1982\)039<2867:ACSOTR>2.0.CO;2](https://doi.org/10.1175/1520-0469(1982)039<2867:ACSOTR>2.0.CO;2), 1982.
- 710 Heymsfield, A. J., Schmitt, C., Bansemer, A., and Twohy, C. H.: Improved Representation of Ice Particle Masses Based on Observations in Natural Clouds, *Journal of the Atmospheric Sciences*, 67, 3303–3318, ISSN 0022-4928, 1520-0469, <https://doi.org/10.1175/2010JAS3507.1>, 2010.
- Heymsfield, G. M., Bidwell, S. W., Caylor, I. J., Ameen, S., Nicholson, S., Boncyk, W., Miller, L., Vandemark, D., Racette, P. E., and Dod, L. R.: The EDOP Radar System on the High-Altitude NASA ER-2 Aircraft, *Journal of Atmospheric and Oceanic Technology*, 13, 795–809, ISSN 0739-0572, 1520-0426, [https://doi.org/10.1175/1520-0426\(1996\)013<0795:TERSOT>2.0.CO;2](https://doi.org/10.1175/1520-0426(1996)013<0795:TERSOT>2.0.CO;2), 1996.
- 715 Heymsfield, G. M., Li, L., and McLinden, M.: ER-2 X-Band Doppler Radar (EXRAD) IMPACTS. Dataset available online from the NASA Global Hydrometeorology Resource Center DAAC, Huntsville, Alabama, U.S.A. , <https://doi.org/10.5067/IMPACTS/EXRAD/DATA101>, <http://dx.doi.org/10.5067/IMPACTS/EXRAD/DATA101>, 2022.
- Houze, R. A., McMurdie, L. A., Petersen, W. A., Schwaller, M. R., Baccus, W., Lundquist, J. D., Mass, C. F., Nijssen, B., Rutledge, S. A., Hudak, D. R., Tanelli, S., Mace, G. G., Poellot, M. R., Lettenmaier, D. P., Zagrodnik, J. P., Rowe, A. K., DeHart, J. C., Madaus, L. E., Barnes, H. C., and Chandrasekar, V.: The Olympic Mountains Experiment (OLYMPEX), *Bulletin of the American Meteorological Society*, 98, 2167–2188, ISSN 0003-0007, 1520-0477, <https://doi.org/10.1175/BAMS-D-16-0182.1>, 2017.
- 720 King, W. D., Parkin, D. A., and Handsworth, R. J.: A Hot-Wire Liquid Water Device Having Fully Calculable Response Characteristics, *Journal of Applied Meteorology and Climatology*, 17, 1809–1813, ISSN 1520-0450, [https://doi.org/10.1175/1520-0450\(1978\)017<1809:AHWLWD>2.0.CO;2](https://doi.org/10.1175/1520-0450(1978)017<1809:AHWLWD>2.0.CO;2), 1978.
- 725

- Kirschler, S., Voigt, C., Anderson, B. E., Chen, G., Crosbie, E. C., Ferrare, R. A., Hahn, V., Hair, J. W., Kaufmann, S., Moore, R. H., Painemal, D., Robinson, C. E., Sanchez, K. J., Scarino, A. J., Shingler, T. J., Shook, M. A., Thornhill, K. L., Winstead, E. L., Ziemba, L. D., and Sorooshian, A.: Overview and Statistical Analysis of Boundary Layer Clouds and Precipitation over the Western North Atlantic Ocean, *Atmospheric Chemistry and Physics*, 23, 10731–10750, ISSN 1680-7316, <https://doi.org/10.5194/acp-23-10731-2023>, 2023.
- 730 Kneifel, S. and Moisseev, D.: Long-Term Statistics of Riming in Nonconvective Clouds Derived from Ground-Based Doppler Cloud Radar Observations, *Journal of the Atmospheric Sciences*, 77, 3495–3508, ISSN 0022-4928, 1520-0469, <https://doi.org/10.1175/JAS-D-20-0007.1>, 2020.
- Korolev, A. and Milbrandt, J.: How Are Mixed-Phase Clouds Mixed?, *Geophysical Research Letters*, 49, e2022GL099578, ISSN 1944-8007, <https://doi.org/10.1029/2022GL099578>, 2022.
- 735 Korolev, A., Emery, E., and Creelman, K.: Modification and Tests of Particle Probe Tips to Mitigate Effects of Ice Shattering, *Journal of Atmospheric and Oceanic Technology*, 30, 690–708, ISSN 0739-0572, 1520-0426, <https://doi.org/10.1175/JTECH-D-12-00142.1>, 2013.
- Korolev, A., McFarquhar, G., Field, P. R., Franklin, C., Lawson, P., Wang, Z., Williams, E., Abel, S. J., Axisa, D., Borrmann, S., Crosier, J., Fugal, J., Krämer, M., Lohmann, U., Schlenczek, O., Schnaiter, M., and Wendisch, M.: Mixed-Phase Clouds: Progress and Challenges, *Meteorological Monographs*, 58, 5.1–5.50, <https://doi.org/10.1175/AMSMONOGRAPHS-D-17-0001.1>, 2017.
- 740 Korolev, A. V., Strapp, J. W., Isaac, G. A., and Nevzorov, A. N.: The Nevzorov Airborne Hot-Wire LWC–TWC Probe: Principle of Operation and Performance Characteristics, *Journal of Atmospheric and Oceanic Technology*, 15, 1495–1510, ISSN 0739-0572, 1520-0426, [https://doi.org/10.1175/1520-0426\(1998\)015<1495:TNAHWL>2.0.CO;2](https://doi.org/10.1175/1520-0426(1998)015<1495:TNAHWL>2.0.CO;2), 1998.
- Korolev, A. V., Isaac, G. A., Cober, S. G., Strapp, J. W., and Hallett, J.: Microphysical Characterization of Mixed-Phase Clouds, *Quarterly Journal of the Royal Meteorological Society*, 129, 39–65, ISSN 1477-870X, <https://doi.org/10.1256/qj.01.204>, 2003.
- 745 Kostinski, A. B. and Jameson, A. R.: On the Spatial Distribution of Cloud Particles, *Journal of the Atmospheric Sciences*, 57, 901–915, ISSN 0022-4928, 1520-0469, [https://doi.org/10.1175/1520-0469\(2000\)057<0901:OTSDOC>2.0.CO;2](https://doi.org/10.1175/1520-0469(2000)057<0901:OTSDOC>2.0.CO;2), 2000.
- Kostinski, A. B. and Shaw, R. A.: Scale-Dependent Droplet Clustering in Turbulent Clouds, *Journal of Fluid Mechanics*, 434, 389–398, ISSN 1469-7645, 0022-1120, <https://doi.org/10.1017/S0022112001004001>, 2001.
- Lance, S., Brock, C. A., Rogers, D., and Gordon, J. A.: Water Droplet Calibration of the Cloud Droplet Probe (CDP) and in-Flight Performance in Liquid, Ice and Mixed-Phase Clouds during ARCPAC, *Atmospheric Measurement Techniques*, 3, 1683–1706, ISSN 1867-1381, <https://doi.org/10.5194/amt-3-1683-2010>, 2010.
- 750 Lawson, P., Gurganus, C., Woods, S., and Bruintjes, R.: Aircraft Observations of Cumulus Microphysics Ranging from the Tropics to Midlatitudes: Implications for a “New” Secondary Ice Process, *Journal of the Atmospheric Sciences*, 74, 2899 – 2920, <https://doi.org/10.1175/JAS-D-17-0033.1>, <https://journals.ametsoc.org/view/journals/atsc/74/9/jas-d-17-0033.1.xml>, 2017.
- 755 Lawson, R. P., Stewart, R. E., and Angus, L. J.: Observations and Numerical Simulations of the Origin and Development of Very Large Snowflakes, *Journal of the Atmospheric Sciences*, 55, 3209–3229, ISSN 0022-4928, 1520-0469, [https://doi.org/10.1175/1520-0469\(1998\)055<3209:OANSOT>2.0.CO;2](https://doi.org/10.1175/1520-0469(1998)055<3209:OANSOT>2.0.CO;2), 1998.
- Lawson, R. P., O’Connor, D., Zmarzly, P., Weaver, K., Baker, B., Mo, Q., and Jonsson, H.: The 2D-S (Stereo) Probe: Design and Preliminary Tests of a New Airborne, High-Speed, High-Resolution Particle Imaging Probe, *Journal of Atmospheric and Oceanic Technology*, 23, 1462–1477, ISSN 0739-0572, 1520-0426, <https://doi.org/10.1175/JTECH1927.1>, 2006.
- 760 Li, L., Heymsfield, G., Carswell, J., Schaubert, D. H., McLinden, M. L., Creticos, J., Perrine, M., Coon, M., Cervantes, J. I., Vega, M., Guimond, S., Tian, L., and Emory, A.: The NASA High-Altitude Imaging Wind and Rain Airborne Profiler, *IEEE Transactions on Geoscience and Remote Sensing*, 54, 298–310, ISSN 1558-0644, <https://doi.org/10.1109/TGRS.2015.2456501>, 2016.

- Li, L., McLinden, M., and Heymsfield, G. M.: High Altitude Imaging Wind and Rain Airborne Profiler (HIWRAP) IMPACTS. Dataset available online from the NASA Global Hydrometeorology Resource Center DAAC, Huntsville, Alabama, U.S.A. , <https://doi.org/10.5067/IMPACTS/HIWRAP/DATA101>, <http://dx.doi.org/10.5067/IMPACTS/HIWRAP/DATA101>, 2022.
- 765 Lucke, J., Jurkat-Witschas, T., Heller, R., Hahn, V., Hamman, M., Breitfuss, W., Bora, V. R., Moser, M., and Voigt, C.: Icing Wind Tunnel Measurements of Supercooled Large Droplets Using the 12 Mm Total Water Content Cone of the Nevzorov Probe, *Atmospheric Measurement Techniques*, 15, 7375–7394, ISSN 1867-1381, <https://doi.org/10.5194/amt-15-7375-2022>, 2022.
- 770 Lucke, J., Moser, M., De La Torre Castro, E., Mayer, J., and Voigt, C.: Nevzorov LWC and TWC data from the HALO-AC3 campaign in March and April 2022, <https://doi.org/10.1594/PANGAEA.963628>, <https://doi.org/10.1594/PANGAEA.963628>, 2024.
- Maahn, M. and Löhnert, U.: Potential of Higher-Order Moments and Slopes of the Radar Doppler Spectrum for Retrieving Microphysical and Kinematic Properties of Arctic Ice Clouds, *Journal of Applied Meteorology and Climatology*, 56, 263–282, ISSN 1558-8424, 1558-8432, <https://doi.org/10.1175/JAMC-D-16-0020.1>, 2017.
- 775 Maahn, M., Löhnert, U., Kollias, P., Jackson, R. C., and McFarquhar, G. M.: Developing and Evaluating Ice Cloud Parameterizations for Forward Modeling of Radar Moments Using in Situ Aircraft Observations, *Journal of Atmospheric and Oceanic Technology*, 32, 880–903, ISSN 0739-0572, 1520-0426, <https://doi.org/10.1175/JTECH-D-14-00112.1>, 2015.
- Maherndl, N., Maahn, M., Tridon, F., Leinonen, J., Ori, D., and Kneifel, S.: A Riming-Dependent Parameterization of Scattering by Snowflakes Using the Self-Similar Rayleigh–Gans Approximation, *Quarterly Journal of the Royal Meteorological Society*, 149, 3562–
780 3581, ISSN 1477-870X, <https://doi.org/10.1002/qj.4573>, 2023a.
- Maherndl, N., Maahn, M., Tridon, F., Leinonen, J., Ori, D., and Kneifel, S.: Data set of simulated rimed aggregates for "A riming-dependent parameterization of scattering by snowflakes using the self-similar Rayleigh-Gans approximation", <https://doi.org/10.5281/zenodo.7757034>, <https://doi.org/10.5281/zenodo.7757034>, 2023b.
- Maherndl, N., Moser, M., Lucke, J., Mech, M., Risse, N., Schirmacher, I., and Maahn, M.: Quantifying riming from airborne data during
785 the HALO-(AC)³ campaign, *Atmospheric Measurement Techniques*, 17, 1475–1495, <https://doi.org/10.5194/amt-17-1475-2024>, <https://amt.copernicus.org/articles/17/1475/2024/>, 2024.
- Mason, S. L., Chiu, C. J., Hogan, R. J., Moisseev, D., and Kneifel, S.: Retrievals of Riming and Snow Density From Vertically Pointing Doppler Radars, *Journal of Geophysical Research: Atmospheres*, 123, 13,807–13,834, ISSN 2169-8996, <https://doi.org/10.1029/2018JD028603>, 2018.
- 790 McLinden, M., Li, L., and Heymsfield, G. M.: Cloud Radar System (CRS) IMPACTS. Dataset available online from the NASA Global Hydrometeorology Resource Center DAAC, Huntsville, Alabama, U.S.A. , <https://doi.org/10.5067/IMPACTS/CRS/DATA101>, <http://dx.doi.org/10.5067/IMPACTS/CRS/DATA101>, 2022.
- McLinden, M. L. W., Li, L., Heymsfield, G. M., Coon, M., and Emory, A.: The NASA GSFC 94-GHz Airborne Solid-State Cloud Radar System (CRS), *Journal of Atmospheric and Oceanic Technology*, 38, 1001–1017, ISSN 0739-0572, 1520-0426,
795 <https://doi.org/10.1175/JTECH-D-20-0127.1>, 2021.
- McMurdie, L. A., Heymsfield, G., Yorks, J. E., and Braun, S. A.: Investigation of Microphysics and Precipitation for Atlantic Coast-Threatening Snowstorms (IMPACTS) Collection. Data available online [<http://ghrc.nsstc.nasa.gov/>] from the NASA EOSDIS Global Hydrology Resource Center Distributed Active Archive Center, Huntsville, Alabama, U.S.A , <https://doi.org/10.5067/IMPACTS/DATA101>, <http://dx.doi.org/10.5067/IMPACTS/DATA101>, 2019.
- 800 McMurdie, L. A., Heymsfield, G. M., Yorks, J. E., Braun, S. A., Skofronick-Jackson, G., Rauber, R. M., Yuter, S., Colle, B., McFarquhar, G. M., Poellot, M., Novak, D. R., Lang, T. J., Kroodsma, R., McLinden, M., Oue, M., Kollias, P., Kumjian, M. R., Greybush, S. J., Heyms-

- field, A. J., Finlon, J. A., McDonald, V. L., and Nicholls, S.: Chasing Snowstorms: The Investigation of Microphysics and Precipitation for Atlantic Coast-Threatening Snowstorms (IMPACTS) Campaign, *Bulletin of the American Meteorological Society*, 103, E1243–E1269, ISSN 0003-0007, 1520-0477, <https://doi.org/10.1175/BAMS-D-20-0246.1>, 2022.
- 805 Mech, M., Kliesch, L.-L., Anhäuser, A., Rose, T., Kollias, P., and Crewell, S.: Microwave Radar/Radiometer for Arctic Clouds (MiRAC): First Insights from the ACLOUD Campaign, *Atmospheric Measurement Techniques*, 12, 5019–5037, ISSN 1867-1381, <https://doi.org/10.5194/amt-12-5019-2019>, 2019.
- Mech, M., Maahn, M., Kneifel, S., Ori, D., Orlandi, E., Kollias, P., Schemann, V., and Crewell, S.: PAMTRA 1.0: The Passive and Active Microwave Radiative TRANSfer Tool for Simulating Radiometer and Radar Measurements of the Cloudy Atmosphere, *Geoscientific Model Development*, 13, 4229–4251, ISSN 1991-959X, <https://doi.org/10.5194/gmd-13-4229-2020>, 2020.
- 810 Mech, M., Ehrlich, A., Herber, A., Lüpkes, C., Wendisch, M., Becker, S., Boose, Y., Chechin, D., Crewell, S., Dupuy, R., Gourbeyre, C., Hartmann, J., Jäkel, E., Jourdan, O., Kliesch, L.-L., Klingebiel, M., Kulla, B. S., Mioche, G., Moser, M., Risse, N., Ruiz-Donoso, E., Schäfer, M., Stapf, J., and Voigt, C.: MOSAiC-ACA and AFLUX - Arctic Airborne Campaigns Characterizing the Exit Area of MOSAiC, *Scientific Data*, 9, 790, ISSN 2052-4463, <https://doi.org/10.1038/s41597-022-01900-7>, 2022a.
- 815 Mech, M., Risse, N., Marrollo, G., and Paul, D.: ac3airborne, <https://doi.org/10.5281/zenodo.7305586>, <https://doi.org/10.5281/zenodo.7305586>, 2022b.
- Mech, M., Risse, N., Krobot, P., Paul, D., Schirmacher, I., Schnitt, S., and Crewell, S.: Radar reflectivities at 94 GHz and microwave brightness temperature measurements at 89 GHz during the HALO-AC3 Arctic airborne campaign, <https://doi.org/10.1594/PANGAEA.964977>, <https://doi.org/10.1594/PANGAEA.964977>, 2024a.
- 820 Mech, M., Risse, N., Ritter, C., Schirmacher, I., and Schween, J. H.: Cloud mask and cloud top altitude from the AMALi airborne lidar on Polar 5 during HALO-AC3 in spring 2022, <https://doi.org/10.1594/PANGAEA.964985>, <https://doi.org/10.1594/PANGAEA.964985>, 2024b.
- Mitchell, D. L.: Use of Mass- and Area-Dimensional Power Laws for Determining Precipitation Particle Terminal Velocities, *Journal of the Atmospheric Sciences*, 53, 1710–1723, ISSN 0022-4928, 1520-0469, [https://doi.org/10.1175/1520-0469\(1996\)053<1710:UOMAAD>2.0.CO;2](https://doi.org/10.1175/1520-0469(1996)053<1710:UOMAAD>2.0.CO;2), 1996.
- 825 0469(1996)053<1710:UOMAAD>2.0.CO;2, 1996.
- Moisseev, D., von Lerber, A., and Tiira, J.: Quantifying the Effect of Riming on Snowfall Using Ground-Based Observations, *Journal of Geophysical Research: Atmospheres*, 122, 4019–4037, ISSN 2169-8996, <https://doi.org/10.1002/2016JD026272>, 2017.
- Morrison, H. and Milbrandt, J. A.: Parameterization of Cloud Microphysics Based on the Prediction of Bulk Ice Particle Properties. Part I: Scheme Description and Idealized Tests, *Journal of the Atmospheric Sciences*, 72, 287–311, ISSN 0022-4928, 1520-0469, <https://doi.org/10.1175/JAS-D-14-0065.1>, 2015.
- 830 Morrison, H., de Boer, G., Feingold, G., Harrington, J., Shupe, M. D., and Sulia, K.: Resilience of Persistent Arctic Mixed-Phase Clouds, *Nature Geoscience*, 5, 11–17, ISSN 1752-0908, <https://doi.org/10.1038/ngeo1332>, 2012.
- Morrison, H., van Lier-Walqui, M., Fridlind, A. M., Grabowski, W. W., Harrington, J. Y., Hoose, C., Korolev, A., Kumjian, M. R., Milbrandt, J. A., Pawlowska, H., Posselt, D. J., Prat, O. P., Reimel, K. J., Shima, S.-I., van Diedenhoven, B., and Xue, L.: Confronting the Challenge of Modeling Cloud and Precipitation Microphysics, *Journal of Advances in Modeling Earth Systems*, 12, e2019MS001689, ISSN 1942-2466, <https://doi.org/10.1029/2019MS001689>, 2020.
- 835 Moser, M., Lucke, J., De La Torre Castro, E., Mayer, J., and Voigt, C.: DLR in situ cloud measurements during HALO-(AC)³ Arctic airborne campaign, <https://doi.org/10.1594/PANGAEA.963247>, <https://doi.org/10.1594/PANGAEA.963247>, 2023.

- Moser, M., Voigt, C., Jurkat-Witschas, T., Hahn, V., Mioche, G., Jourdan, O., Dupuy, R., Gourbeyre, C., Schwarzenboeck, A., Lucke, J.,
840 Boose, Y., Mech, M., Borrmann, S., Ehrlich, A., Herber, A., Lüpkes, C., and Wendisch, M.: Microphysical and Thermodynamic Phase
Analyses of Arctic Low-Level Clouds Measured above the Sea Ice and the Open Ocean in Spring and Summer, *Atmospheric Chemistry
and Physics*, 23, 7257–7280, ISSN 1680-7316, <https://doi.org/10.5194/acp-23-7257-2023>, 2023.
- Mróz, K., Battaglia, A., Kneifel, S., von Terzi, L., Karrer, M., and Ori, D.: Linking Rain into Ice Microphysics across the Melting Layer in
845 Stratiform Rain: A Closure Study, *Atmospheric Measurement Techniques*, 14, 511–529, ISSN 1867-1381, <https://doi.org/10.5194/amt-14-511-2021>, 2021.
- Mülmenstädt, J., Sourdeval, O., Delanoë, J., and Quaas, J.: Frequency of Occurrence of Rain from Liquid-, Mixed-, and Ice-
Phase Clouds Derived from A-Train Satellite Retrievals, *Geophysical Research Letters*, 42, 6502–6509, ISSN 1944-8007,
<https://doi.org/10.1002/2015GL064604>, 2015.
- Nguyen, C. M., Wolde, M., Battaglia, A., Nichman, L., Bliankinshtein, N., Haimov, S., Bala, K., and Schuettemeyer, D.: Coincident in Situ
850 and Triple-Frequency Radar Airborne Observations in the Arctic, *Atmospheric Measurement Techniques*, 15, 775–795, ISSN 1867-1381,
<https://doi.org/10.5194/amt-15-775-2022>, 2022.
- Ong, C. R., Koike, M., Hashino, T., and Miura, H.: Responses of Simulated Arctic Mixed-Phase Clouds to Parameterized Ice Particle Shape,
Journal of the Atmospheric Sciences, 81, 125–152, ISSN 0022-4928, 1520-0469, <https://doi.org/10.1175/JAS-D-23-0015.1>, 2024.
- Petters, M. D. and Wright, T. P.: Revisiting Ice Nucleation from Precipitation Samples, *Geophysical Research Letters*, 42, 8758–8766, ISSN
855 1944-8007, <https://doi.org/10.1002/2015GL065733>, 2015.
- Rodgers, C. D.: *Inverse Methods for Atmospheric Sounding: Theory and Practice*, World Scientific, <https://doi.org/10.1142/3171>, 2000.
- Ruiz-Donoso, E., Ehrlich, A., Schäfer, M., Jäkel, E., Schemann, V., Crewell, S., Mech, M., Kulla, B. S., Kliesch, L.-L., Neuber, R., and
860 Wendisch, M.: Small-Scale Structure of Thermodynamic Phase in Arctic Mixed-Phase Clouds Observed by Airborne Remote Sensing
during a Cold Air Outbreak and a Warm Air Advection Event, *Atmospheric Chemistry and Physics*, 20, 5487–5511, ISSN 1680-7316,
<https://doi.org/10.5194/acp-20-5487-2020>, 2020.
- Saw, E.-W., Salazar, J. P. L. C., Collins, L. R., and Shaw, R. A.: Spatial Clustering of Polydisperse Inertial Particles in Turbulence: I. Compar-
ing Simulation with Theory, *New Journal of Physics*, 14, 105 030, ISSN 1367-2630, <https://doi.org/10.1088/1367-2630/14/10/105030>,
2012a.
- Saw, E.-W., Shaw, R. A., Salazar, J. P. L. C., and Collins, L. R.: Spatial Clustering of Polydisperse Inertial Particles in Turbulence: II. Compar-
865 ing Simulation with Experiment, *New Journal of Physics*, 14, 105 031, ISSN 1367-2630, <https://doi.org/10.1088/1367-2630/14/10/105031>,
2012b.
- Schirmacher, I., Kollias, P., Lamer, K., Mech, M., Pfitzenmaier, L., Wendisch, M., and Crewell, S.: Assessing Arctic Low-Level
Clouds and Precipitation from above – a Radar Perspective, *Atmospheric Measurement Techniques*, 16, 4081–4100, ISSN 1867-1381,
<https://doi.org/10.5194/amt-16-4081-2023>, 2023.
- 870 Schirmacher, et al.: Clouds and precipitation in the initial phase of marine cold air outbreaks as observed by airborne remote sensing [in
prep.], 2024.
- Seifert, A., Leinonen, J., Siewert, C., and Kneifel, S.: The Geometry of Rimed Aggregate Snowflakes: A Modeling Study, *Journal of Adv-
ances in Modeling Earth Systems*, 11, 712–731, ISSN 1942-2466, <https://doi.org/10.1029/2018MS001519>, 2019.
- Shaw, R. A., Kostinski, A. B., and Larsen, M. L.: Towards Quantifying Droplet Clustering in Clouds, *Quarterly Journal of the Royal Meteo-
875 rological Society*, 128, 1043–1057, ISSN 1477-870X, <https://doi.org/10.1256/003590002320373193>, 2002.

- Shupe, M. D. and Intrieri, J. M.: Cloud Radiative Forcing of the Arctic Surface: The Influence of Cloud Properties, Surface Albedo, and Solar Zenith Angle, *Journal of Climate*, 17, 616–628, ISSN 0894-8755, 1520-0442, [https://doi.org/10.1175/1520-0442\(2004\)017<0616:CRFOTA>2.0.CO;2](https://doi.org/10.1175/1520-0442(2004)017<0616:CRFOTA>2.0.CO;2), 2004.
- 880 Sorooshian, A., Alexandrov, M. D., Bell, A. D., Bennett, R., Betito, G., Burton, S. P., Buzanowicz, M. E., Cairns, B., Chemyakin, E. V., Chen, G., Choi, Y., Collister, B. L., Cook, A. L., Corral, A. F., Crosbie, E. C., van Dierenhoven, B., DiGangi, J. P., Diskin, G. S., Dmitrovic, S., Edwards, E.-L., Fenn, M. A., Ferrare, R. A., van Gilst, D., Hair, J. W., Harper, D. B., Hilario, M. R. A., Hostetler, C. A., Jester, N., Jones, M., Kirschler, S., Kleb, M. M., Kusterer, J. M., Leavor, S., Lee, J. W., Liu, H., McCauley, K., Moore, R. H., Nied, J., Notari, A., Nowak, J. B., Painemal, D., Phillips, K. E., Robinson, C. E., Scarino, A. J., Schlosser, J. S., Seaman, S. T., Seethala, C., Shingler, T. J., Shook, M. A., Sinclair, K. A., Smith Jr., W. L., Spangenberg, D. A., Stamnes, S. A., Thornhill, K. L., Voigt, C., Vömel, H., Wasilewski, A. P.,
- 885 Wang, H., Winstead, E. L., Zeider, K., Zeng, X., Zhang, B., Ziemba, L. D., and Zuidema, P.: Spatially Coordinated Airborne Data and Complementary Products for Aerosol, Gas, Cloud, and Meteorological Studies: The NASA ACTIVATE Dataset, *Earth System Science Data*, 15, 3419–3472, ISSN 1866-3508, <https://doi.org/10.5194/essd-15-3419-2023>, 2023.
- Stachlewska, I. S., Neuber, R., Lampert, A., Ritter, C., and Wehrle, G.: AMALi – the Airborne Mobile Aerosol Lidar for Arctic Research, *Atmospheric Chemistry and Physics*, 10, 2947–2963, ISSN 1680-7316, <https://doi.org/10.5194/acp-10-2947-2010>, 2010.
- 890 Sun, Z. and Shine, K. P.: Studies of the Radiative Properties of Ice and Mixed-Phase Clouds, *Quarterly Journal of the Royal Meteorological Society*, 120, 111–137, ISSN 1477-870X, <https://doi.org/10.1002/qj.49712051508>, 1994.
- Toohey, D., Noone, D., and Wein, E.: Water Isotope System for Precipitation and Entrainment Research (WISPER) IMPACTS. Dataset available online from the NASA Global Hydrometeorology Resource Center DAAC, Huntsville, Alabama, U.S.A. , <https://doi.org/10.5067/IMPACTS/WISPER/DATA101>, <http://dx.doi.org/10.5067/IMPACTS/WISPER/DATA101>, 2022.
- 895 Tridon, F., Battaglia, A., Chase, R. J., Turk, F. J., Leinonen, J., Kneifel, S., Mroz, K., Finlon, J., Bansemmer, A., Tanelli, S., Heymsfield, A. J., and Nesbitt, S. W.: The Microphysics of Stratiform Precipitation During OLYMPEX: Compatibility Between Triple-Frequency Radar and Airborne In Situ Observations, *Journal of Geophysical Research: Atmospheres*, 124, 8764–8792, ISSN 2169-8996, <https://doi.org/10.1029/2018JD029858>, 2019.
- Tridon, F., Silber, I., Battaglia, A., Kneifel, S., Fridlind, A., Kalogeras, P., and Dhillon, R.: Highly Supercooled Riming and Unusual
- 900 Triple-Frequency Radar Signatures over Antarctica, *Atmospheric Chemistry and Physics Discussions*, pp. 1–34, ISSN 1680-7316, <https://doi.org/10.5194/acp-2022-136>, 2022.
- Turner, D. D.: Arctic Mixed-Phase Cloud Properties from AERI Lidar Observations: Algorithm and Results from SHEBA, *Journal of Applied Meteorology and Climatology*, 44, 427–444, ISSN 1520-0450, 0894-8763, <https://doi.org/10.1175/JAM2208.1>, 2005.
- Waitz, F., Schnaiter, M., Leisner, T., and Järvinen, E.: In Situ Observation of Riming in Mixed-Phase Clouds Using the PHIPS Probe,
- 905 *Atmospheric Chemistry and Physics*, 22, 7087–7103, ISSN 1680-7316, <https://doi.org/10.5194/acp-22-7087-2022>, 2022.
- Walbröl, A., Michaelis, J., Becker, S., Dorff, H., Ebell, K., Gorodetskaya, I., Heinold, B., Kirbus, B., Lauer, M., Mahernndl, N., Maturilli, M., Mayer, J., Müller, H., Neggers, R. A. J., Paulus, F. M., Röttenbacher, J., Rückert, J. E., Schirmacher, I., Slättberg, N., Ehrlich, A., Wendisch, M., and Crewell, S.: Contrasting extremely warm and long-lasting cold air anomalies in the North Atlantic sector of the Arctic during the HALO-(AC)³ campaign, *Atmospheric Chemistry and Physics*, 24, 8007–8029, <https://doi.org/10.5194/acp-24-8007-2024>,
- 910 <https://acp.copernicus.org/articles/24/8007/2024/>, 2024.
- Wendisch, M., Crewell, S., Ehrlich, A., Herber, A., Kirbus, B., Lüpkes, C., Mech, M., Abel, S. J., Akansu, E. F., Ament, F., Aubry, C., Becker, S., Borrmann, S., Bozem, H., Brückner, M., Clemen, H.-C., Dahlke, S., Dekoutsidis, G., Delanoë, J., De La Torre Castro, E., Dorff, H., Dupuy, R., Eppers, O., Ewald, F., George, G., Gorodetskaya, I. V., Grawe, S., Groß, S., Hartmann, J., Henning, S., Hirsch, L., Jäkel, E.,

- 915 Joppe, P., Jourdan, O., Jurányi, Z., Karalis, M., Kellermann, M., Klingebiel, M., Lonardi, M., Lucke, J., Luebke, A., Maahn, M., Maherndl, N., Maturilli, M., Mayer, B., Mayer, J., Mertes, S., Michaelis, J., Michalkov, M., Mioche, G., Moser, M., Müller, H., Neggers, R., Ori, D., Paul, D., Paulus, F., Pilz, C., Pithan, F., Pöhlker, M., Pörtge, V., Ringel, M., Risse, N., Roberts, G. C., Rosenburg, S., Röttenbacher, J., Rückert, J., Schäfer, M., Schäfer, J., Schemann, V., Schirmacher, I., Schmidt, J., Schmidt, S., Schneider, J., Schnitt, S., Schwarz, A., Siebert, H., Sodemann, H., Sperzel, T., Spreen, G., Stevens, B., Stratmann, F., Svensson, G., Tatzelt, C., Tuch, T., Vihma, T., Voigt, C., Volkmer, L., Walbröl, A., Weber, A., Wehner, B., Wetzel, B., Wirth, M., and Zinner, T.: Overview: Quasi-Lagrangian observations of Arctic air mass transformations – Introduction and initial results of the HALO–(AC)³ aircraft campaign, *EGUsphere*, 2024, 1–46, <https://doi.org/10.5194/egusphere-2024-783>, <https://egusphere.copernicus.org/preprints/2024/egusphere-2024-783/>, 2024.
- 920 Wood, A. M., Hwang, W., and Eaton, J. K.: Preferential Concentration of Particles in Homogeneous and Isotropic Turbulence, *International Journal of Multiphase Flow*, 31, 1220–1230, ISSN 0301-9322, <https://doi.org/10.1016/j.ijmultiphaseflow.2005.07.001>, 2005.